UNIVERSITÀ DEGLI STUDI DI GENOVA

SCUOLA POLITECNICA

DIME

Dipartimento di Ingegneria Meccanica, Energetica, Gestionale e dei Trasporti

MASTER OF SCIENCE THESIS
IN
MECHANICAL ENGINEERING

Homogenization of phoretic flows through micro-structured surfaces

Supervisors:

Chiar.^{mo} Prof. Ing. Alessandro Bottaro

Dr. Giuseppe Antonio Zampogna

Chiar.^{mo} Prof. Ing. François Gallaire

Candidate:
Edoardo Carlo Giordano

March 2023

Acknowledgements

I miei ringraziamenti vanno ai miei relatori, il Prof. Bottaro, il Prof. Gallaire e il Dr. Zampogna. Il primo per avermi offerto l'opportunità di svolgere la tesi all'estero credendo nelle mie capacità. Il secondo per avermi accolto all'interno del suo laboratorio. Infine, il Dr. Zampogna per avermi seguito quotinianamente nel progetto, trasmettendomi la sua passione per la ricerca e aiutandomi a superare ogni ostacolo incontrato durante la realizzazione della tesi.

Grazie anche a tutti i colleghi del laboratorio, per avermi accolto e messo a mio agio e, soprattutto, per avermi insegnato tanto. In particolare Kevin per essere stato un punto di riferimento e Yves-Marie per essere stato sempre disponibile ad aiutarmi.

Ci tengo a ringraziare in particolare i miei genitori e le mie sorelle, Sofia e Irene, per non aver mai fatto mancare il loro sostegno, non avrei ottenuto questi risultati se non ci fosse stato il loro supporto.

Un grazie a Matteo, Cristiano, Federico, Edoardo, Francesco, Davide e Andrea per essere venuti a trovarmi nonostante la distanza.

Un ringraziamento particolare a Simone e Stefano per essere sempre al mio fianco.

Ringrazio Alberto e Giacomo per essere stati la mia famiglia in questi mesi all'estero.

Infine ci tengo a ricordare le persone che non ci sono piu' ma che sicuramente avrebbero festeggiato con me questo traguardo. Mio Nonno Giovanni, Massimo, Nazareno, Adriano, Yonny e il mio caro amico Andrea.

Omogenizzazione di flussi foretici attraverso superfici micro-strutturate

Sommario

Le superficie foretiche suscitano particolare attenzione tra la comunità accademica impegnata nel campo dell'idrodinamica chimico-fisica, in quanto permettono di generare e modificare flussi all'interno di dispositivi microfluidici come microcanali. In questa tesi, un modello multiscala per l'analisi di flussi attraverso membrane microstrutturate permeabili, formate da un materiale foretico, è stato sviluppato tramite una tecnica di omogeneizzazione. Il modello afferma che la velocità del solvente e la concentrazione del soluto alla membrana sono proporzionali agli sforzi fluidi e ai flussi di soluto calcolati sui lati opposti della membrana. Nelle condizioni che definiscono la velocità del solvente e la concentrazione del soluto, il modello contiene un ulteriore contributo foretico, che trova le sue origini nell'interazione microscopica tra la tripla solvente-soluto-struttura solida. La soluzione del modello è stata implementata numericamente per svariate configurazioni di flusso. Dopo una validazione del nuovo set di equazioni attraverso il confronto con la soluzione di equazioni che rappresentano i principi primi che governano il fenomeno, è stato mostrato come, variando le proprietà micro- e macroscopiche della struttura foretica, è possibile generare flussi con caratteristiche differenti.

Homogenization of phoretic flows through micro-structured surfaces

Abstract

Phoretic surfaces are attracting particular attention among the academic community engaged in the field of physicochemical hydrodynamics. These surfaces represent a reliable strategy to generate and modify flows within microfluidic devices such as microchannels. In this thesis, a multiscale model to analyze flows through permeable microstructured membranes formed by a phoretic material is developed using a homogenization technique. The model states the existence of a jump in the solvent stresses and solute fluxes across the membrane, quantified by the solution of microscopic problems solved in the vicinity of one single solid inclusion forming the membrane. Among the others, some coefficients represent an additional phoretic contribution to the solvent stress and solute flux jumps, which find their origins in the microscopic interactions between the solvent, the solute, and the solid structure. The solution of the model is found for several flow configurations, via its FEM-based numerical implementation. After validation of the new set of equations by comparisons with the solution of the first-principles governing the physics, it has been shown how the variations of the micro- and macroscopic properties of the phoretic structure affect the flow behaviour.

Contents

1 Introduction

Controlled flow manipulation at the micro- or nanoscale is the core of recent developments in microfluidics, including many applications in the field of biological analysis and screening [1]. Generating and controlling a flow within the confined environment of a microfluidic device require an external forcing to overcome the viscous stress on the walls [2]. In microfluidic channels, this is usually achieved, by applying a hydrodynamic or osmotic pressure difference between the inlet and outlet of the domain. However, many biological systems rely on forcing localized in the vicinity of the internal boundaries of the system itself, rather than on a global volumetric forcing. Microscopic cilia on the lung epithelium induce a directional flow of mucus through their coordinated beating, acting as a pump [3]. Several attempts have been made to artificially reproduce ciliary pumping through the fabrication of actuated cilia [4, 5] and the challenges deriving from miniaturization are still open [6, 7, 8]. Phoretic mechanisms, namely the ability to generate fluid motion near a boundary under the effect of an external concentration gradient, represent an alternative way for pumping systems that require no moving parts. Phoresis arises from the interaction between solid surfaces and chemical solute species. Phoretic motion has recently received renewed attention in the context of artificial selfpropelled bodies. Such artificial swimmers generate the concentration gradient required to propel themselves, for example through chemical reactions catalyzed at their surface [9, 10, 11, 12, 13].

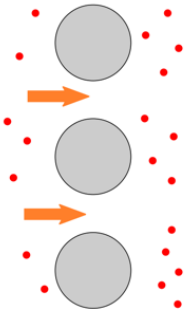

Fig. 1.1: Phoresis effect in the vicinity of an array of circular particles (in grey). A two-component mixture of a solvent and a solute is considered. The red dots represent the solute particles. Phoresis generates a solvent flow represented by orange arrows.

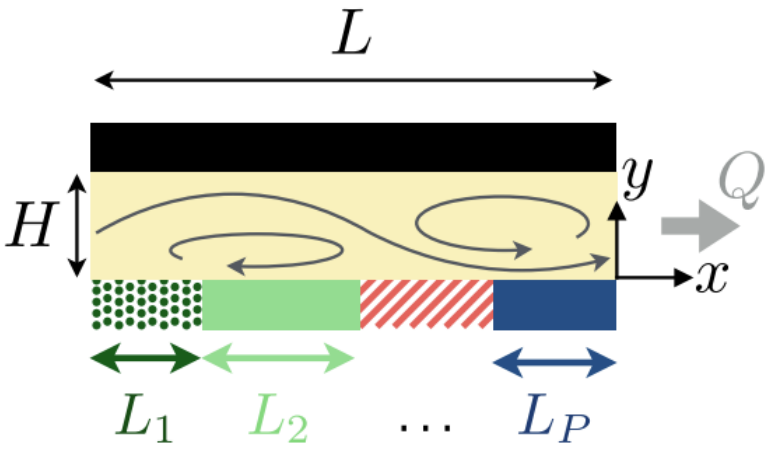

Fig. 1.2: Periodic phoretic pump design: A straight, two-dimensional channel of width H is periodically coated with P chemically-active patches (per period L) of lengths L_1, L_2, ..., L_P (transverse stripes in three dimensions). Phoresis leads to a flow of rate Q (schematic flow illustration).[14]

An example of a phoresis-based pump in a microfluidic channel can be found in [14]. The authors considered an infinite two-dimensional channel of height H (cf. figure 1.2). The wall located at y=0 is chemically-coated with a catalyst along a repeated pattern of period L. The catalyst allows a chemical reactant in the liquid to produce a new solute species of concentration c(x). In the limit of large reactant concentration, they assumed that the solute release occurs at a fixed rate, or activity, A(x), i.e.

$$D\frac{\partial c}{\partial y}\,|_{y=0} = -A(x). \tag{1.1}$$

Local surface gradients in solute concentration result in a net slip velocity providing an effective slip boundary condition for the flow velocity, **u**:

$$(\mathbf{u}\cdot\mathbf{e}_x)\,|_{y=0} = M(x)\frac{\partial c}{\partial x}\,|_{y=0} \tag{1.2}$$

with M(x) the local phoretic mobility along the wall.
In opposition to this simplified, single scale design, multiscale phoretic surfaces have been considered [15].

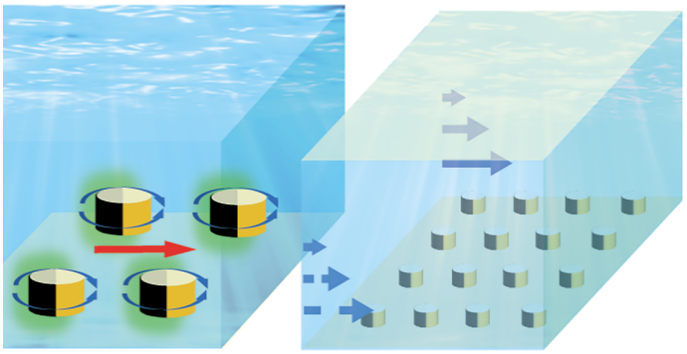

Fig. 1.3: Periodic distribution of phoretic pillars on a smooth surface. Each pillar acts as chemically powered micro-pumps, generating a bulk flow. [15]

The surface designed in [15] is one of the many possible strategies to realize phoretic pumps in a channel (cf. figure 1.3). One could imagine to build thin porous structures, i.e. membranes, by a concatenation of phoretic particles.

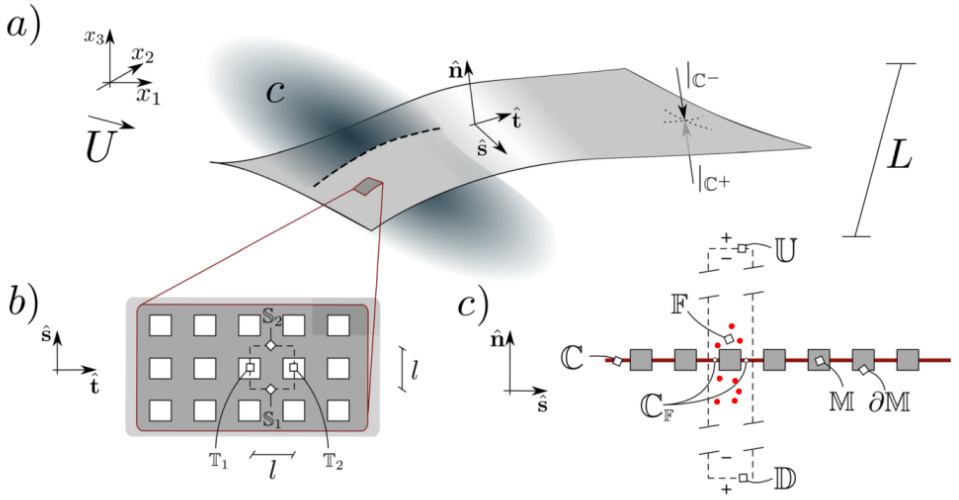

Fig. 1.4: Fluid flow encountering a thin permeable membrane. The fluid is a two-component mixture of a solvent and a solute, the red dots. (a) From a macroscopic point of view the micro-perforated surface corresponds to a fictitious wall denoted with $\mathbb{C}$, provided with a local frame of reference $(\hat{\boldsymbol{s}},\hat{\boldsymbol{t}},\hat{\boldsymbol{n}})$. We define the upward side of the membrane as the side of $\mathbb{C}$ whose outer normal coincides with $\hat{\boldsymbol{n}}$ in the sketch, counter imposed on the downward opposite side. Its size along the tangential directions $\hat{\boldsymbol{s}}$ and $\hat{\boldsymbol{t}}$ is of order L. (b) Zoom in on the plane $(\hat{\boldsymbol{s}},\hat{\boldsymbol{t}})$. The pores form a periodic pattern realized by the repetition of the microscopic cell represented by the dashed square. (c) Zoom in on the plane $(\hat{\boldsymbol{t}}, \hat{\boldsymbol{n}})$ of a portion of the membrane with an example of microscopic elementary cell (dashed rectangle). [16]

In the present thesis, a framework to analyze phoretic multiscale structures is developed using a homogenization technique [17], whose workflow is sketched in figure 1.5 . The outcome of the procedure is a macroscopic condition to be imposed over a thin homogeneous interface between two fluid regions (grey smooth surface in figure 1.4a).

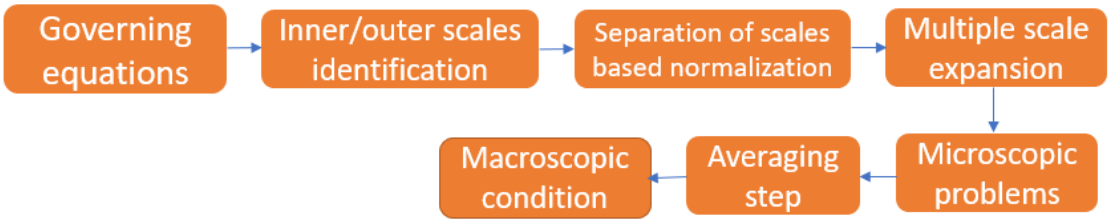

Fig. 1.5: Diagram of the procedure used to deduce the macroscopic interface condition to describe phoretic flows through microstructured permeable walls. The main steps of homogenization are listed.

1.1 Thesis content

In the present thesis we first define the equations governing phoretic flows through microstructured membranes in the short and long range potential hypothesis (chapter 2). We then homogenize the short range potential equations in chapter 3. In chapter 4, we analyze the solution of the microscopic problems found during the homogenization procedure, while in chapter 5 we exploit the microscopic results to solve for several macroscopic configurations. In the same chapter, the macroscopic results are validated against fully resolved direct numerical simulations (DNS) of the flow fields. In chapter 6, we homogenize the long range potential equations. In chapter 7, we analyze the solution of the microscopic problems for these new set of equations. In chapter 8, we consider a test configuration for the macroscopic model developed in chapter 6. In chapter 9, the conclusions and perspectives of the work are discussed.

2 Problem definition

We consider a diluted solute advected by the flow of a newtonian fluid, the solvent, encountering a microstructured permeable surface, the membrane. The solute concentration and diffusivity are denoted by $\hat{c}$ and D while the solvent density and viscosity by ρ and μ. The dimensional velocity $\hat{u}_i$ and pressure $\hat{p}$ in the fluid domain $\mathbb{F}$ are governed by the Navier–Stokes equations. We define ϕ as the chemical potential while k_b is the Boltzmann constant and T the absolute temperature of the medium.
The solute concentration is governed by the advection-diffusion equation i.e.

$$\rho\hat{\partial}_t u_i + \rho\hat{u}_j\hat{\partial}_j u_i = -\hat{\partial}_i\hat{p} + \mu\hat{\partial}^2_{ll}\hat{u}_i - \hat{c}\hat{\partial}_i k_b T\phi \ , \quad \hat{\partial}_i\hat{u}_i = 0 \ , \tag{2.1}$$

$$\hat{\partial}_t\hat{c} + \hat{\partial}_i\hat{F}_i = 0 \ , \tag{2.2}$$

where $\hat{F}_i$ is the concentration flux

$$\hat{F}_i = \hat{u}_i\hat{c} - D(\hat{\partial}_i\hat{c} + \hat{c}\hat{\partial}_i\phi) \ . \tag{2.3}$$

The following boundary conditions are imposed on the membrane walls denoted with $\partial\mathbb{M}$

$$\hat{u}^s_i = 0 \tag{2.4}$$

$$\alpha\hat{F}_i n_i = \beta\hat{c} + \gamma\hat{A}(\hat{x}) \tag{2.5}$$

where α, β and γ are parameters allowing to consider different kinds of solute-structure interactions such as imposed concentration value ($\alpha = \gamma = 0$ and $\beta = 1$), or imposed concentration flux ($\alpha = \beta = 1$ and $\gamma = 0$).

2.1 Chemical potential

The chemical potential ϕ describes the interaction between the solute and the solvent in the vicinity of the membrane. Its range of action λ typically reaches a distance from the solid surface which spans from 0.5 to 200 nm [18].

2.2 Short range potential

When the range λ of the potential is small with respect to the pore size, we introduce the definition of short range potential. We introduce δ, the non dimensional range of action of ϕ, as

$$\delta = \frac{\lambda}{l - a} \tag{2.6}$$

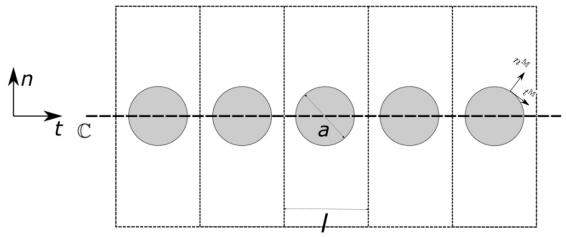

Fig. 2.1: Zoom on an array of solid inclusions forming a membrane. l is the tangential to the membrane width of the microscopic cell and a is the diameter of the inclusions.

If $\delta \ll 1$, all phoretic effects on the solvent are bundled into a boundary condition for the solvent velocity on $\partial\mathbb{M}$, namely the slip velocity due to tangential solute gradients, i.e.

$$\hat{u}_i^{ph} = \hat{M}(\delta_{ij} - n_i^{\mathbb{M}} n_j^{\mathbb{M}}) \cdot \partial_j c \tag{2.7}$$

with the local mobility M defined from the local interaction potential profile and $n^{\mathbb{M}}$ the normal to the solid inclusions (cf. fig. 2.1). The governing equations are describing the solvent-solute couple:

$$\begin{cases} \rho\hat{\partial}_t u_i + \rho\hat{u}_j\hat{\partial}_j u_i = -\hat{\partial}_i\hat{p} + \mu\hat{\partial}_{ll}^2\hat{u}_i \\ \hat{\partial}_i\hat{u}_i = 0 \\ \partial_{\hat{t}}\hat{c} + \hat{\partial}_i\hat{F}_i = 0 \\ \hat{F}_i = \hat{u}_i\hat{c} - D(\hat{\partial}_i\hat{c}) \\ \hat{u}_i^s = \hat{M}(\delta_{ij} - n_i^{\mathbb{M}} n_j^{\mathbb{M}}) \cdot \partial_j c \text{ on } \partial\mathbb{M} \\ \alpha\hat{F}_i n_i = \beta\hat{c} + \gamma\hat{A}(\hat{x}) \text{ on } \partial\mathbb{M} \end{cases} \tag{2.8}$$

2.3 Long range potential

According to [19], if $\delta \approx 1$, we are in the case of the long range potential hypothesis and the full system of equations (2.1, 2.2, 2.3, 2.4, 2.5) has to be homogenized to find the macroscopic interface condition valid on the smooth grey surface of figure 1.4a.

3 Homogenization of the short range potential equations

In this section we develop a set of equations describing the macroscopic behavior of the solvent-solute couple across the phoretic structure in the short range potential limit. The problem is characterised by two different scales: the characteristic size of the entire phoretic structure, L, and the typical size of the pores, l, as sketched in figure (2.1). The relation between l and L defines a small parameter

$$\varepsilon := \frac{l}{L} \ll 1. \tag{3.1}$$

We introduce two different sets of representative scales.
For the outer problem valid far from the membrane, outside the microscopic elementary cell (cf. figure 3.1), we have

$$c^* = \Delta C^{\mathbb{O}} c^{\mathbb{O}} \ , \quad \hat{x} = L x^{\mathbb{O}} \ , \quad \hat{p} = \Delta P p^{\mathbb{O}} \ , \quad \hat{u} = U^{\mathbb{O}} u^{\mathbb{O}} = \frac{L \Delta P}{\mu} \mathbf{u}^{\mathbb{O}} \tag{3.2}$$

For the inner problem valid within the microscopic elementary cell (cf. figure 3.1), the following relations hold

$$c^* = \Delta C^{\mathbb{I}} c^{\mathbb{I}} \ , \quad \hat{x} = l x^{\mathbb{I}} \ , \quad \hat{p} = \Delta P p^{\mathbb{I}} \ , \quad \hat{u} = U^{\mathbb{I}} u^{\mathbb{I}} = \frac{l \Delta P}{\mu} \mathbf{u}^{\mathbb{I}} \ , \quad \hat{M} = \frac{U^{\mathbb{I}}}{l \Delta C^{\mathbb{I}}} \ . \tag{3.3}$$

In the inner domain the dimensionless equations read

$$\begin{cases} Re_l u_j^{\mathbb{I}} \partial_j u_i^{\mathbb{I}} = -\partial_i p^{\mathbb{I}} + \partial_{ll}^2 u_i^{\mathbb{I}} \\ \partial_i u_i^{\mathbb{I}} = 0 \\ \partial_i F_i^{\mathbb{I}} = 0 \\ F_i^{\mathbb{I}} = Pe^{\mathbb{I}} u_i^{\mathbb{I}} c^{\mathbb{I}} - D(\partial_i c^{\mathbb{I}}) \\ u_i^s = M(\delta_{ij} - n_i^{\mathbb{M}} n_j^{\mathbb{M}}) \cdot \partial_j c \ \text{ on } \partial\mathbb{M} \\ \alpha F_i n_i = \beta c + \gamma A(x) \ \text{ on } \partial\mathbb{M}, \end{cases} \tag{3.4}$$

with $Re_l = \frac{\rho U^{\mathbb{I}} l}{\mu}$ and $Pe^{\mathbb{I}} = \frac{U^{\mathbb{I}} l}{D}$. Following the procedure sketched in figure 1.5, we introduce the fast (microscopic) and slow (macroscopic) variables, $\mathrm{x} = (x_s, x_t, x_n)$ and $\mathrm{X} = \varepsilon(x_s, x_t, x_n)$. The unknown variables are decomposed as

$$\mathbf{u}^{\mathbb{I}} = \sum_{n=0}^{+\infty} \varepsilon^n \mathbf{u}^{\mathbb{I},n}(\mathbf{x}, \mathbf{X}, t) \ , \quad p^{\mathbb{I}} = \sum_{n=0}^{+\infty} \varepsilon^n p^{\mathbb{I},n}(\mathbf{x}, \mathbf{X}, t) \ , \quad c^{\mathbb{I}} = \sum_{n=0}^{+\infty} \varepsilon^n c^{\mathbb{I},n}(\mathbf{x}, \mathbf{X}, t) \ . \tag{3.5}$$

The spatial derivatives are transformed following the rule

$$\partial_i \to \partial_i + \varepsilon \partial_I \ . \tag{3.6}$$

In the outer region there is no need to introduce the expansion since the flow depends only on X. Substituting equations (3.5, 3.6) into equation (3.4) and collecting the leading order terms, we obtain

$$\begin{cases} -\partial_i p^{\mathbb{I},0} + \partial^2_{ll} u_i^{\mathbb{I},0} = 0 \\ \partial_i u_i^{\mathbb{I},0} = 0 \\ \partial_i F_i^{\mathbb{I},0} = 0 \\ F_i^{\mathbb{I}} = -\partial_i c^{\mathbb{I},0} \end{cases} \tag{3.7}$$

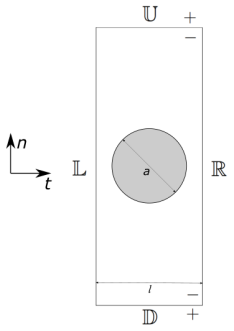

Fig. 3.1: Sketch of the microscopic domain.

since we assumed that Re_l and $Pe^{\mathbb{I}}$ are of order ε [16]. Equations (3.7) are solved within the microscopic domain sketched in figure 3.1, whose boundary conditions on $\mathbb{U}$ and $\mathbb{D}$ are

$$\begin{cases} \hat{u}_i^- = \hat{u}_i^+ \\ \hat{\Sigma}_{jk}^- n_k = \hat{\Sigma}_{jk}^+ n_k \\ \hat{c}^- = \hat{c}^+ \\ \hat{F}_i^- n_i = \hat{F}_i^+ n_i, \end{cases} \tag{3.8}$$

plus periodicity on $\mathbb{L}$ and $\mathbb{R}$. The superscript $+$ denotes the outer region while $-$ denotes the inner region (cf. figure 3.1).
Normalizing equations (3.8), as specified by equations (3.2) and (3.3) we obtain

$$\Sigma_{jk}^{\mathbb{O}} n_k = [-\frac{\Delta P^{\mathbb{U},\mathbb{D}}}{\Delta P} p^{\mathbb{O}} \delta_{jk} + 2\frac{U^{\mathbb{U},\mathbb{D}}}{L\Delta P} \mu \varepsilon_{jk}(\mathbf{u}^{\mathbb{O}})] n_k \tag{3.9}$$

$$F_i^{\mathbb{I}} n_i = F_i^{\mathbb{O}} n_i \text{ on } \mathbb{U} \text{ and } \mathbb{D} \, . \tag{3.10}$$

3.1 Solution of the microscopic problem

Since problem (3.7, 3.9) is linear, we can write its solution as

$$u_i^{\mathbb{I},0} = M_{ijk}\Sigma_{jk}^{\mathbb{O},\mathbb{U}} + N_{ijk}\Sigma_{jk}^{\mathbb{O},\mathbb{D}} + u_i^{ph} \tag{3.11}$$

$$p^{\mathbb{I},0} = Q_{jk}\Sigma_{jk}^{\mathbb{O},\mathbb{U}} + R_{jk}\Sigma_{jk}^{\mathbb{O},\mathbb{D}} + p^{ph} \tag{3.12}$$

$$c^{\mathbb{I},0} = T_i F_i^{\mathbb{O},\mathbb{U}} + Y_i F_i^{\mathbb{O},\mathbb{D}} + c^{ph} \tag{3.13}$$

where **M**, **N**, **Q**, **R**, **T** and **Y** are unknown tensors and vectors. The slip velocity u_i^{ph} is the phoretic contribution to the velocity. c^{ph} is the phoretic contribution to the concentration field. Substituting (3.11,3.12,3.13) into the leading order problem (3.7) and the boundary condition (3.9), we obtain the systems of equations (3.14) and (3.15) that can be solved to obtain **M**, **N**, **Q**, **R**, **T**, **Y**, u_i^{ph}, p^{ph} and c^{ph}, i.e.

$$\begin{cases} -\partial_i Q_{jk} + \partial_{ll}^2 M_{ijk} = 0 \text{ in } \mathbb{F} \\ \partial_i M_{ijk} = 0 \text{ in } \mathbb{F} \\ M_{ijk} = 0 \text{ on } \partial\mathbb{M} \\ \sum_{pq}(M_{\cdot jk}, Q_{jk})n_q = \delta_{jp}\delta_{kq}n_q \text{ on } \mathbb{U} \\ \sum_{pq}(M_{\cdot jk}, Q_{jk})n_q = 0 \text{ on } \mathbb{D} \\ M_{ijk}, Q_{jk} \text{ periodic along } \hat{t} \text{ and } \hat{s} \end{cases} \qquad \begin{cases} -\partial_i R_{jk} + \partial_{ll}^2 N_{ijk} = 0 \text{ in } \mathbb{F} \\ \partial_i N_{ijk} = 0 \text{ in } \mathbb{F} \\ N_{ijk} = 0 \text{ on } \partial\mathbb{M} \\ \sum_{pq}(N_{\cdot jk}, R_{jk})n_q = 0 \text{ on } \mathbb{U} \\ \sum_{pq}(N_{\cdot jk}, R_{jk})n_q = \delta_{jp}\delta_{kq}n_q \text{ on } \mathbb{D} \\ N_{ijk}, R_{jk} \text{ periodic along } \hat{t} \text{ and } \hat{s} \end{cases}$$

$$\begin{cases} -\partial_i p^{ph} + \partial_{ll}^2 u_i^{ph} = 0 \text{ in } \mathbb{F} \\ \partial_i u_i^{ph} = 0 \text{ in } \mathbb{F} \\ u_i^{ph} = M(\delta_{ij} - n_i^{\mathbb{M}} n_j^{\mathbb{M}}) \cdot \partial_j c \text{ on } \partial\mathbb{M} \\ \sum_{pq}(u_{\cdot jk}^{ph}, p_{jk}^{ph})n_q = 0 \text{ on } \mathbb{D}, \mathbb{U}, \end{cases} \tag{3.14}$$

$$\begin{cases} -\partial_{ii}^2 T_j = 0 \text{ in } \mathbb{F} \\ T_j = 0 \text{ on } \partial\mathbb{M} \\ -\partial_i T_j n_i = n_j \text{ on } \mathbb{U} \\ -\partial_i T_j n_i = 0 \text{ on } \mathbb{D} \\ T_j \text{ periodic along } \hat{t} \text{ and } \hat{s} \end{cases} \qquad \begin{cases} -\partial_{ii}^2 Y_j = 0 \text{ in } \mathbb{F} \\ Y_j = 0 \text{ on } \partial\mathbb{M} \\ -\partial_i Y_j n_i = 0 \text{ on } \mathbb{U} \\ -\partial_i Y_j n_i = n_j \text{ on } \mathbb{D} \\ Y_j \text{ periodic along } \hat{t} \text{ and } \hat{s} \end{cases}$$

$$\begin{cases} \partial_{ii}^2 c^{ph} = 0 \text{ in } \mathbb{F} \\ \partial_i c^{ph} n_i^{\mathbb{M}} = \beta c^{ph} + \gamma A(x) \text{ on } \partial\mathbb{M} \\ \partial_n c^{ph} = 0 \text{ on } \mathbb{D}, \mathbb{U}. \end{cases} \tag{3.15}$$

Systems (3.14) are forced by an ensemble of ten independent Navier-Stokes problems, while systems (3.15) are forced by an ensemble of four independent Laplace problems.

3.2 From the microscopic solution to the macroscopic interface condition

To account for the upstream and downstream far-field membrane effects, the upward $\overline{\cdot}^{\mathbb{U}}$ and downward $\overline{\cdot}^{\mathbb{D}}$ averages are defined

$$\overline{\cdot}^{\mathbb{U}} = \lim_{x'_n \to +\infty} \frac{1}{\mathbb{U}} \int_{\mathbb{U}} \cdot dx'_s dx'_t - x'_n \quad \text{and} \quad \overline{\cdot}^{\mathbb{D}} = \lim_{x'_n \to -\infty} \frac{1}{\mathbb{D}} \int_{\mathbb{D}} \cdot dx'_s dx'_t - x'_n. \tag{3.16}$$

Applying the averages to conditions (3.11) and (3.13) we obtain

$$\overline{u}_i^{\mathbb{C}^-} = \overline{u}_i^{\mathbb{U}} = \overline{M}_{ijk}^{\mathbb{U}} \Sigma_{jk}^{\mathbb{C}^-} + \overline{N}_{ijk}^{\mathbb{U}} \Sigma_{jk}^{\mathbb{C}^+} + \overline{u_i^{ph}}^{\mathbb{U}} \tag{3.17}$$

$$\overline{u}_i^{\mathbb{C}^+} = \overline{u}_i^{\mathbb{D}} = \overline{M}_{ijk}^{\mathbb{D}} \Sigma_{jk}^{\mathbb{C}^-} + \overline{N}_{ijk}^{\mathbb{D}} \Sigma_{jk}^{\mathbb{C}^+} + \overline{u_i^{ph}}^{\mathbb{D}} \tag{3.18}$$

$$\overline{c}^{\mathbb{C}^-} = \overline{c}^{\mathbb{U}} = \overline{T}_i^{\mathbb{U}} F_i^{\mathbb{C}^-} + \overline{Y}_i^{\mathbb{U}} F_i^{\mathbb{C}^+} + \overline{c_i^{ph}}^{\mathbb{U}} \tag{3.19}$$

$$\overline{c}^{\mathbb{C}^+} = \overline{c}^{\mathbb{D}} = \overline{T}_i^{\mathbb{D}} F_i^{\mathbb{C}^-} + \overline{Y}_i^{\mathbb{D}} F_i^{\mathbb{C}^+} + \overline{c_i^{ph}}^{\mathbb{D}} \tag{3.20}$$

To write the macroscopic interface condition for the outer problem, we dimensionalise equations (3.17,3.18,3.19,3.20) with (3.3) and then non-dimensionlise with (3.2), i.e.

$$\overline{u}_i^{\mathbb{C}^-} = \overline{u}_i^{\mathbb{U}} = \varepsilon(\overline{M}_{ijk}^{\mathbb{U}} \Sigma_{jk}^{\mathbb{C}^-} + \overline{N}_{ijk}^{\mathbb{U}} \Sigma_{jk}^{\mathbb{C}^+}) + \overline{u_i^{ph}}^{\mathbb{U}} \tag{3.21}$$

$$\overline{u}_i^{\mathbb{C}^+} = \overline{u}_i^{\mathbb{D}} = \varepsilon(\overline{M}_{ijk}^{\mathbb{D}} \Sigma_{jk}^{\mathbb{C}^-} + \overline{N}_{ijk}^{\mathbb{D}} \Sigma_{jk}^{\mathbb{C}^+}) + \overline{u_i^{ph}}^{\mathbb{D}} \tag{3.22}$$

$$\overline{c}^{\mathbb{C}^-} = \overline{c}^{\mathbb{U}} = \varepsilon(\overline{T}_i^{\mathbb{U}} F_i^{\mathbb{C}^-} + \overline{Y}_i^{\mathbb{U}} F_i^{\mathbb{C}^+}) + \overline{c_i^{ph}}^{\mathbb{U}} \tag{3.23}$$

$$\overline{c}^{\mathbb{C}^+} = \overline{c}^{\mathbb{D}} = \varepsilon(\overline{T}_i^{\mathbb{D}} F_i^{\mathbb{C}^-} + \overline{Y}_i^{\mathbb{D}} F_i^{\mathbb{C}^+}) + \overline{c_i^{ph}}^{\mathbb{D}} \tag{3.24}$$

Microscopic problems (3.14, 3.15) are written in the frame of reference (t, s, n) of the macroscopic surface. To exploit equations (3.17, 3.18, 3.19, 3.20) in a general flow configuration, we would like to express (3.14, 3.15) in cartesian terms. To this purpose, we first observe that

$$\begin{cases} u_{t^{\mathbb{M}}} = A \nabla_{t^{\mathbb{M}}} c \\ u_{s^{\mathbb{M}}} = A \nabla_{s^{\mathbb{M}}} c \quad \text{on } \mathbb{M} \\ u_{n^{\mathbb{M}}} = 0 \end{cases} \tag{3.25}$$

where ($t^{\mathbb{M}}$,$s^{\mathbb{M}}$,$n^{\mathbb{M}}$) is the frame of reference of each solid inclusion. The velocities in (3.25) can be written in term of (t, s, n), i.e.

$$\begin{cases} u \cdot t = [u_{t^{\mathbb{M}}} \hat{t}^{\mathbb{M}}(t,s,n) + u_{s^{\mathbb{M}}} \hat{s}^{\mathbb{M}}(t,s,n)] \cdot t \\ u \cdot s = [u_{t^{\mathbb{M}}} \hat{t}^{\mathbb{M}}(t,s,n) + u_{s^{\mathbb{M}}} \hat{s}^{\mathbb{M}}(t,s,n)] \cdot s \\ u \cdot n = [u_{t^{\mathbb{M}}} \hat{t}^{\mathbb{M}}(t,s,n) + u_{s^{\mathbb{M}}} \hat{s}^{\mathbb{M}}(t,s,n)] \cdot n \end{cases} \tag{3.26}$$

To retrace the tensors in the cartesian reference frame we need a coordinate transformation:

$$\overline{M}_{ijk} = \overline{M}_{ttn}\mathbf{t}\wedge\mathbf{t}\wedge\mathbf{n} + \overline{M}_{tnn}\mathbf{t}\wedge\mathbf{n}\wedge\mathbf{n} + \overline{M}_{ntn}\mathbf{n}\wedge\mathbf{t}\wedge\mathbf{n} + \overline{M}_{nnn}\mathbf{n}\wedge\mathbf{n}\wedge\mathbf{n} \quad (3.27)$$

$$\overline{N}_{ijk} = \overline{N}_{ttn}\mathbf{t}\wedge\mathbf{t}\wedge\mathbf{n} + \overline{N}_{tnn}\mathbf{t}\wedge\mathbf{n}\wedge\mathbf{n} + \overline{N}_{ntn}\mathbf{n}\wedge\mathbf{t}\wedge\mathbf{n} + \overline{N}_{nnn}\mathbf{n}\wedge\mathbf{n}\wedge\mathbf{n} \quad (3.28)$$

$$\overline{T}_i = \overline{T}_t\mathbf{t} + \overline{T}_n\mathbf{n} \quad (3.29)$$

$$\overline{Y}_i = \overline{T}_t\mathbf{t} + \overline{T}_n\mathbf{n} \quad (3.30)$$

The same is applied to the phoretic contribution:

$$\overline{u}_i^{ph} = \overline{u}_t^{ph}\mathbf{t} + \overline{u}_n^{ph}\mathbf{n} \quad (3.31)$$

$$\overline{c}^{ph} = \overline{c}_n^{ph}\mathbf{n} \quad (3.32)$$

where ($\mathbf{t}$, $\mathbf{s}$, $\mathbf{n}$) are written in the cartesian frame of reference ($\mathbf{e}_1$, $\mathbf{e}_2$, $\mathbf{e}_3$).

4 Microscopic solution

In this chapter we present the results of problems (3.14, 3.15) for a specific inclusion with diameter $a = 0.7l$ (cf. figure 3.1). The microscopic problems are implemented using Comsol Multiphisics, via the weak form PDE module. We refer to Appendix A1 for further numerical details.

	M_{ttn}	M_{nnn}	T_n	N_{ttn}	N_{nnn}	Y_n
$\dot{\mathbb{U}}$	4.76×10^{-2}	4.98×10^{-3}	7.53×10^{-2}	4.1×10^{-6}	-4.98×10^{-3}	-2.4×10^{-4}
$\dot{\mathbb{D}}$	-4.1×10^{-6}	4.98×10^{-3}	2.4×10^{-4}	-4.76×10^{-2}	-4.98×10^{-3}	-7.53×10^{-2}

Tab. 4.1: Non-zero averaged components of $\mathbf{M}, \mathbf{N}, \mathbf{T}$ *and* $\mathbf{Y}$

Table 4.1 shows the components of the microscopic tensors and vectors whose averages are non-zero. While the corresponding microscopic fields are shown in figure 4.1.

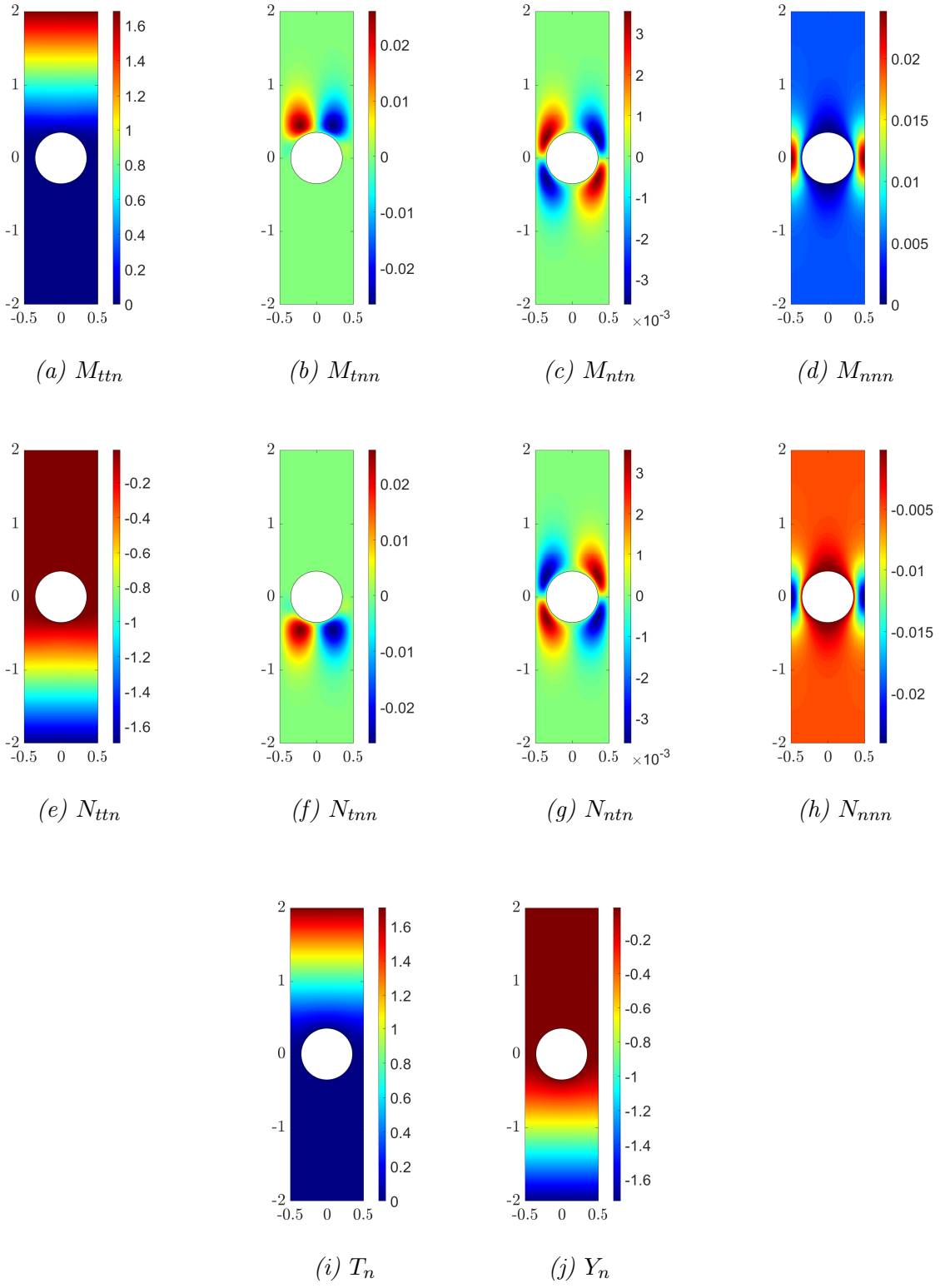

(a) M_{ttn} *(b)* M_{tnn} *(c)* M_{ntn} *(d)* M_{nnn}

(e) N_{ttn} *(f)* N_{tnn} *(g)* N_{ntn} *(h)* N_{nnn}

(i) T_n *(j)* Y_n

Fig. 4.1: Microscopic solution. M_{ttn} *and* M_{tnn} *are obtained imposing tangential stress on* $\mathbb{U}$ *and represent the slip of the membrane.* M_{ntn} *and* M_{nnn} *are obtained imposing a normal stress on* $\mathbb{U}$ *and represent the permeability of the membrane.* T_n *and* Y_n *are the effective diffusivity vectors of the membrane.*

We now consider the solution of (3.14) and (3.15) with $\alpha = 0$, $\beta = 1$ and $\gamma = 1$ with $c\,|_{\partial\mathbb{M}}$ such that

$$A(x) = cos(\theta)t^{\mathbb{M}} + sen(\theta)n^{\mathbb{M}} + 1 \tag{4.1}$$

The results are shown for θ=0°, θ=45°and θ=315°

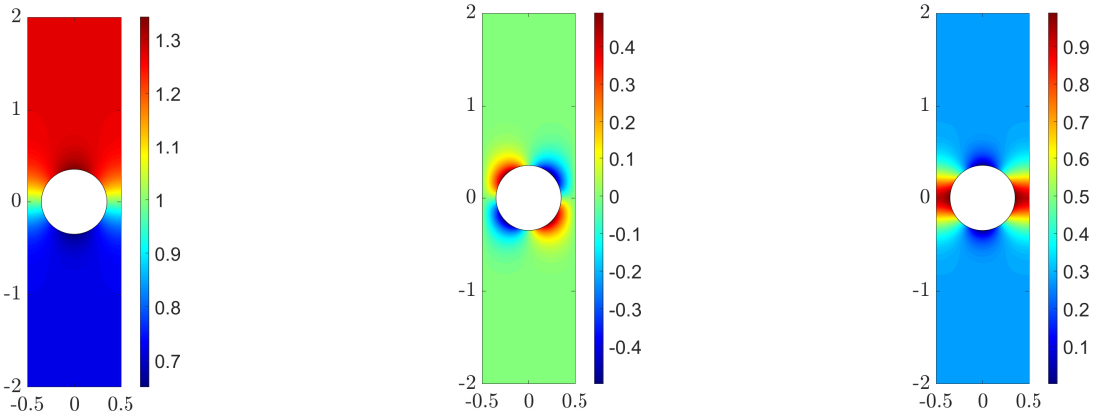

(a) c^{ph} *(b) u_t^{ph}* *(c) u_n^{ph}*

Fig. 4.2: c^{ph} and u^{ph} with $\theta = 0^\circ$ in equation (4.1)

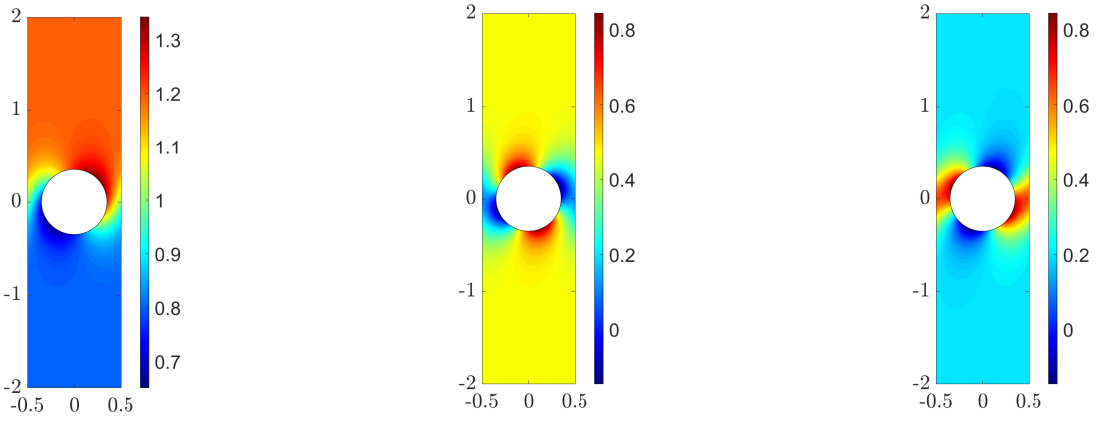

(a) c^{ph} *(b) u_t^{ph}* *(c) u_n^{ph}*

Fig. 4.3: c^{ph} and u^{ph} with $\theta = 45^\circ$ in equation (4.1)

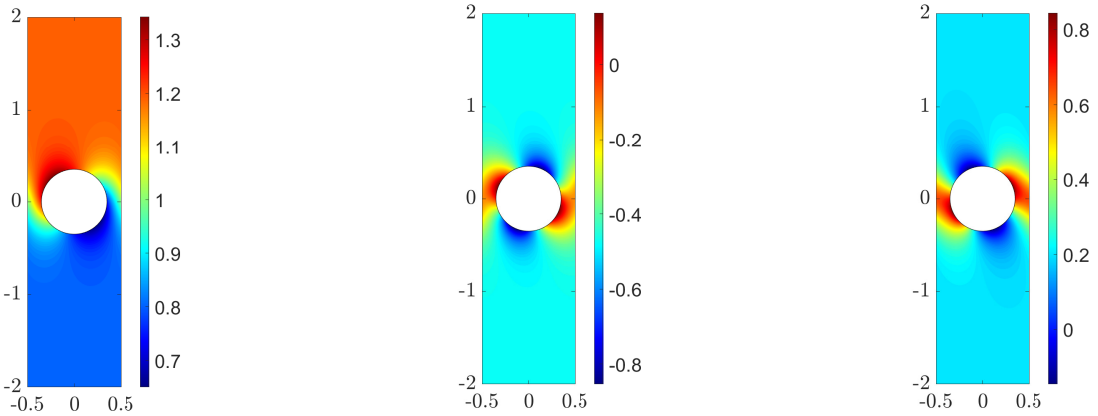

(a) c^{ph} *(b)* u_t^{ph} *(c)* u_n^{ph}

Fig. 4.4: c^{ph} *and* u^{ph} *with* $\theta = 315^\circ$ *in equation (4.1)*

0°	c^{ph}	u_t^{ph}	u_n^{ph}
$\dot{-}\mathbb{U}$	1.27	0	2.86×10^{-1}
$\dot{-}\mathbb{D}$	7.25×10^{-1}	0	2.86×10^{-1}

Tab. 4.2: Average values of c^{ph} *and* u^{ph} *with* $\theta = 0^\circ$.

45°	c^{ph}	u_t^{ph}	u_n^{ph}
$\dot{-}\mathbb{U}$	1.19	4.71×10^{-1}	2.02×10^{-1}
$\dot{-}\mathbb{D}$	8.05×10^{-1}	4.71×10^{-1}	2.02×10^{-1}

Tab. 4.3: Average values of c^{ph} *and* u^{ph} *with* $\theta = 45^\circ$.

315°	c^{ph}	u_t^{ph}	u_n^{ph}
$\dot{-}\mathbb{U}$	1.19	-4.71×10^{-1}	2.02×10^{-1}
$\dot{-}\mathbb{D}$	8.05×10^{-1}	-4.71×10^{-1}	2.02×10^{-1}

Tab. 4.4: Average values of c^{ph} *and* u^{ph} *with* $\theta = 315^\circ$.

5 Macroscopic solution and validation

Once the microscopic quantities have been obtained from problems (3.14, 3.15), it is possible to exploit equations (3.17, 3.18, 3.19) and (3.20) to solve for a macroscopic configuration. The solution of the homogeneous model has been validated by comparisons with the flow field solved at all scales present in the problem.

5.1 Different configurations

We consider a 2D channel as test configuration. A no slip condition is imposed on the upper and lower walls of the channel and no velocity or concentration sources are assumed at the left and right boundaries of the channel, where the mixture freely flows. For every case analysed, we vary the shape of the macroscopic membrane and the boundary condition for the concentration at the membrane.

We show how the flux inside a two-dimensional straight channel changes with the membrane properties. The pure diffusive transport of mass is analysed in section 5.2 to 5.5 while in section 5.6 also non negligible advection is considered ($Pe^{\mathbb{O}} \gg 0$).

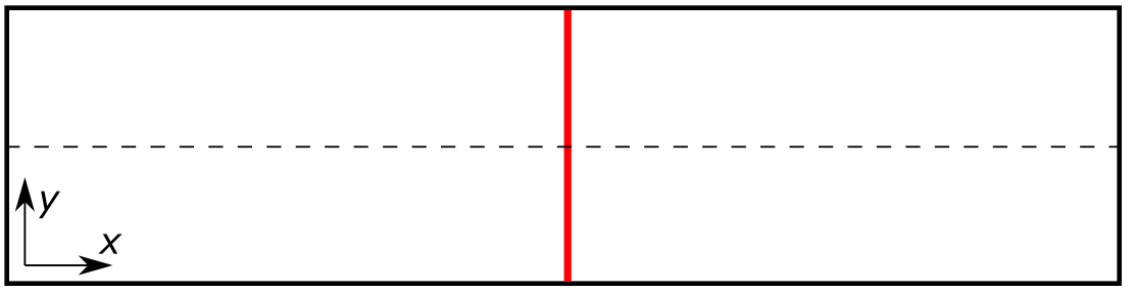

(a) Test configuration case 1

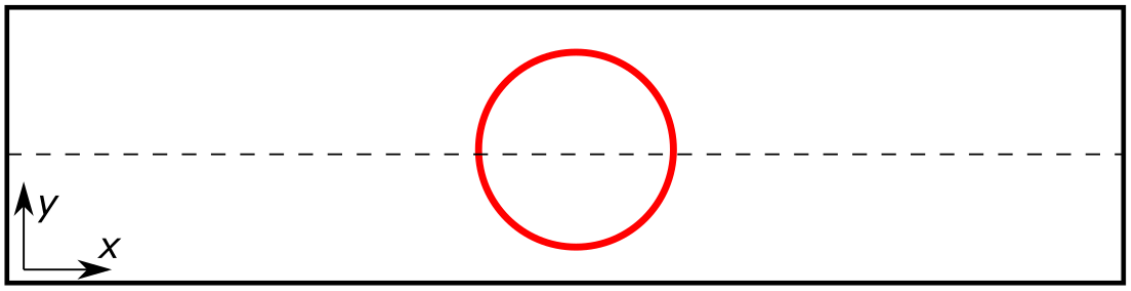

(b) Test configuration case 2

Fig. 5.1: Sketches of the cases considered here; a vertical (a) and circular (b) membrane have been placed within a 2D channel. The red lines represent the membrane, the black lines represent the boundary of the domain and the dashed line is the central line of the channel. The computational domain has length L_y along y and L_x along x.

5.2 Validation Case 1

Case 1 of figure 5.1 is considered. A membrane splits the channel vertically. In this case condition (4.1) with $\theta = 0$ is imposed and a solvent flow is generated. The contours of figure 5.2, depict the concentration c in the channel. The black lines represent the flow streamlines. In the caption, DNS refers to the flow fields solved at all scales present in the problem (equations 3.4), while "macroscopic model" to the solution of equations (3.17–3.20).

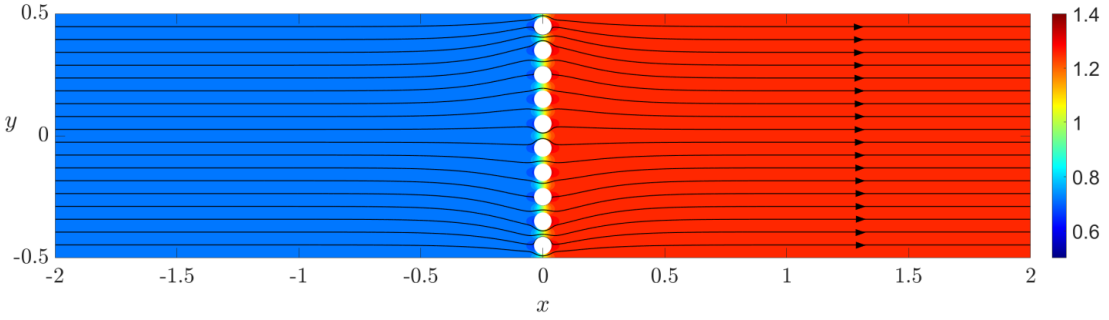

(a) DNS

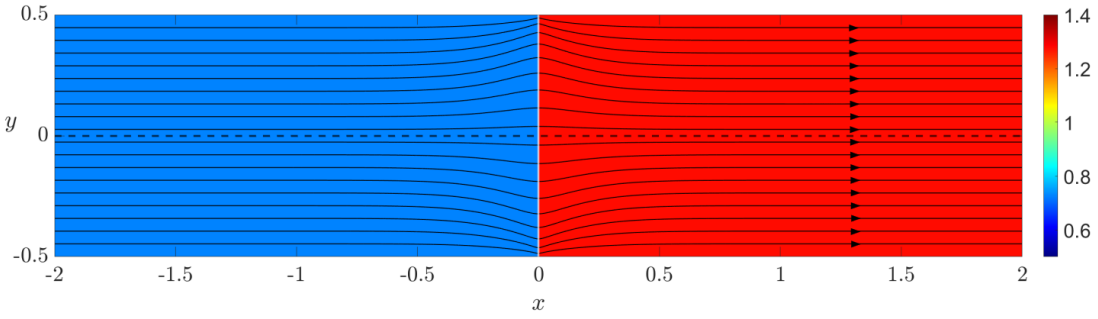

(b) Macroscopic model

Fig. 5.2: Isocontours of concentration with flow streamlines. (a) is the solution of the full-scale equation (3.4). (b) is the solution of the macroscopic model derived via homogenization, (3.17–3.20). The black lines represent the streamlines. In (a) the white circles are the solid inclusions forming the membrane. In (b) the vertical white line represents the equivalent macroscopic membrane.

Three ε values were analysed, $\varepsilon = 0.1, 0.05, 0.025$. As can be seen from figure 5.3, already with the largest ε there is a very good agreement between the DNS and the macroscopic model. The solutions for the other ε are not shown. The relative error on the horizontal velocity on the membrane has been analysed, showing a linear decrease with ε (cf. figure 5.5).

A degradation of the agreement at the upper and lower ends of the membrane is noticed, due to the decay of periodicity in these regions.

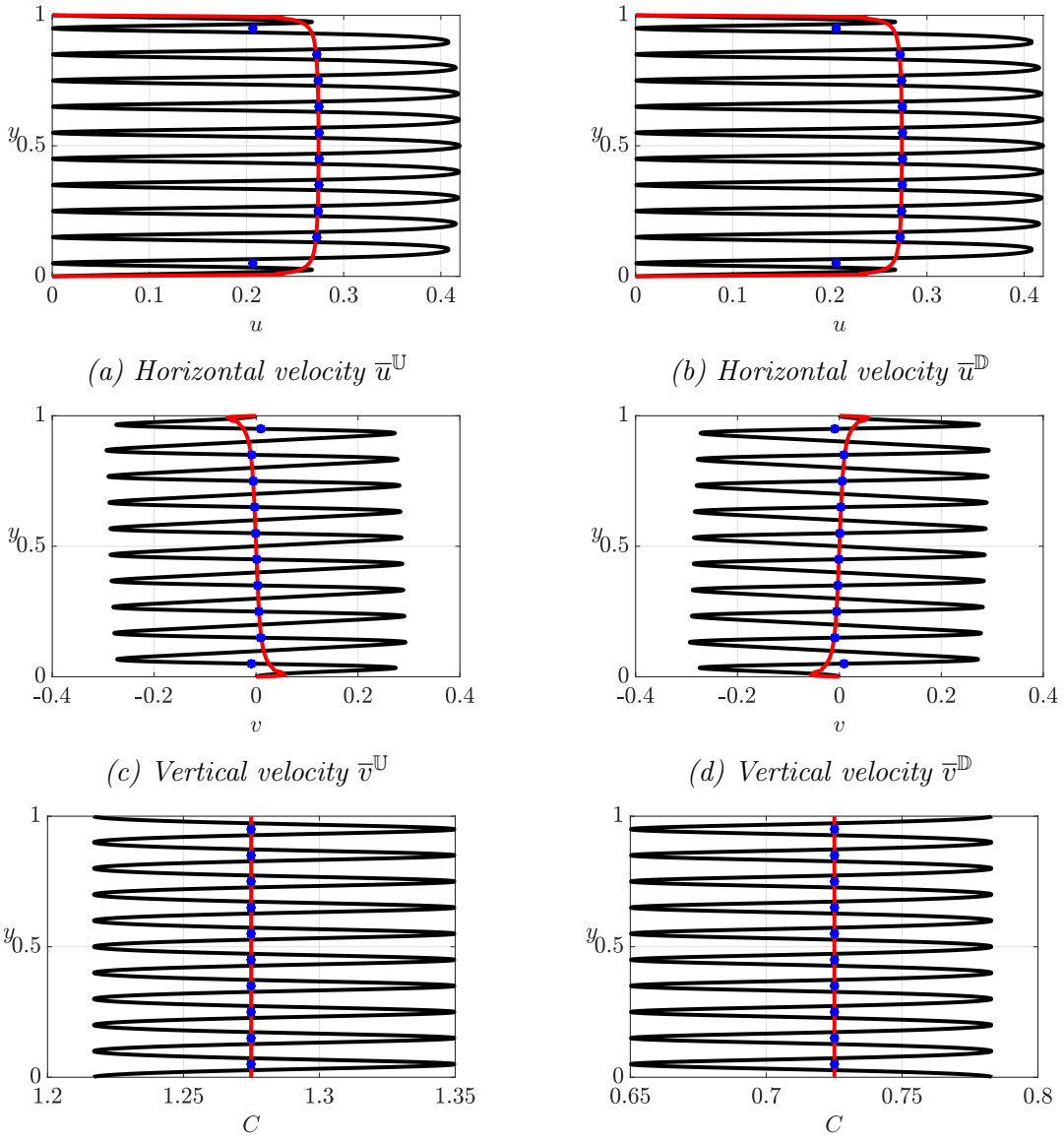

(a) Horizontal velocity $\overline{u}^{\mathbb{U}}$ *(b) Horizontal velocity* $\overline{u}^{\mathbb{D}}$

(c) Vertical velocity $\overline{v}^{\mathbb{U}}$ *(d) Vertical velocity* $\overline{v}^{\mathbb{D}}$

(e) Concentration $\overline{c}^{\mathbb{U}}$ *(f) Concentration* $\overline{c}^{\mathbb{D}}$

Fig. 5.3: Quantitative comparison for ε*=0.1. Horizontal velocities (a,b), vertical velocities (c,d) and concentrations (e,f) have been evaluated along the membrane. Frames (a,c,e) refer to* $\overline{\cdot}^{\mathbb{U}}$ *(3.16). Frames (b,d,f) refer to the* $\overline{\cdot}^{\mathbb{D}}$ *(3.16). Black profiles refer to the solution of full-scale equations (3.4). The solid red lines refer to the solution of the macroscopic model (3.17–3.20). The blue points represent the average of the full-scale solution.*

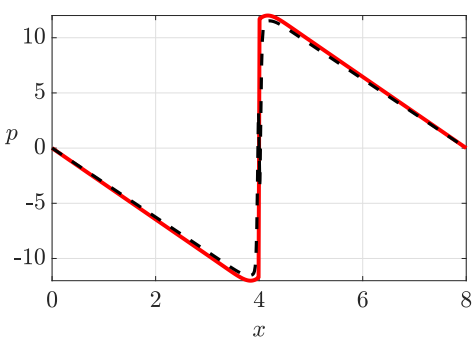

(a) Pressure p

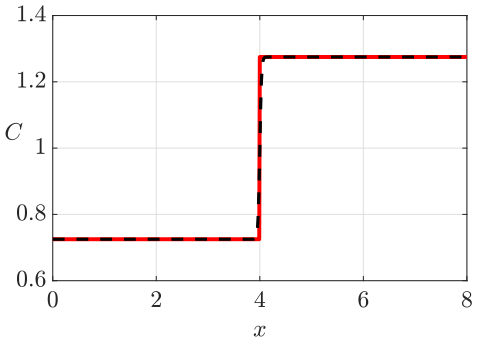

(b) Concentration C

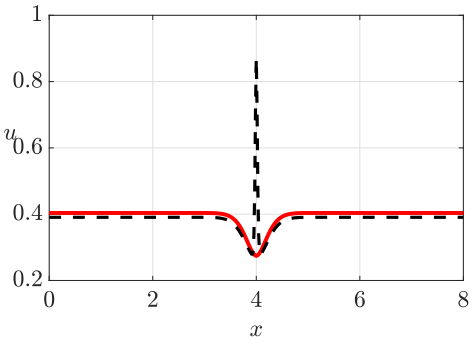

(c) Horizontal velocity u

Fig. 5.4: Quantitative comparison for ε=0.1 over the center line of the channel (horizontal dashed line sketched in figure 5.1). Black profiles refer to the solution of the full-scale equation (3.4). The solid red line refer to the solution of the macroscopic model (3.17–3.20).

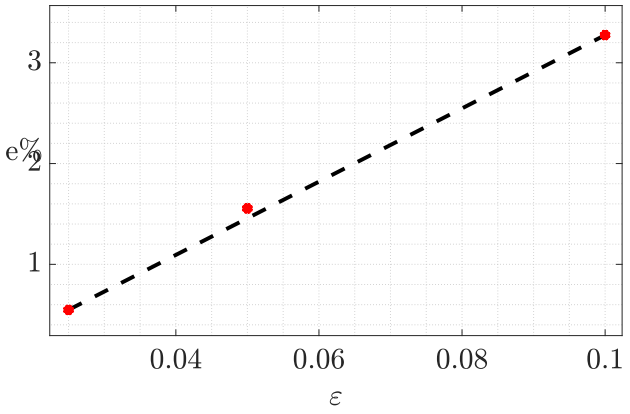

Fig. 5.5: The red points represent $e\% = \frac{|\overline{u}_{dns} - u|}{\frac{\overline{u}+u}{2}} \times 100$ calculated on the central point of the membrane, at $x = \frac{L_x}{2}$ and $y = \frac{L_y}{2}$.

5.3 Validation Case 2

The same geometry of case 1 is considered. The concentration on $\partial\mathbb{M}$ satisfies a Neumann boundary condition with $\alpha = 1$, $\beta = 0$ and $\gamma = 1$ in equation (2.5). The value of $A(x)$ is specified as follows

$$A(x) = n_x + 5, \tag{5.1}$$

where n_x is the horizontal component of the normal vector of the macroscopic membrane $\mathbb{C}$.

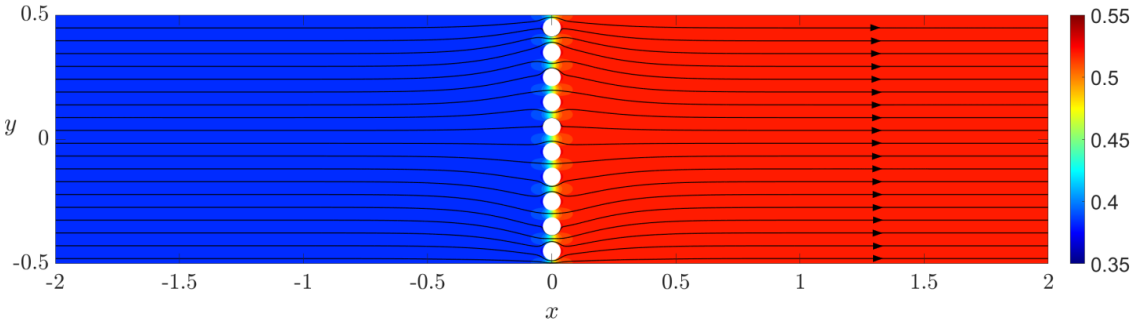

(a) DNS

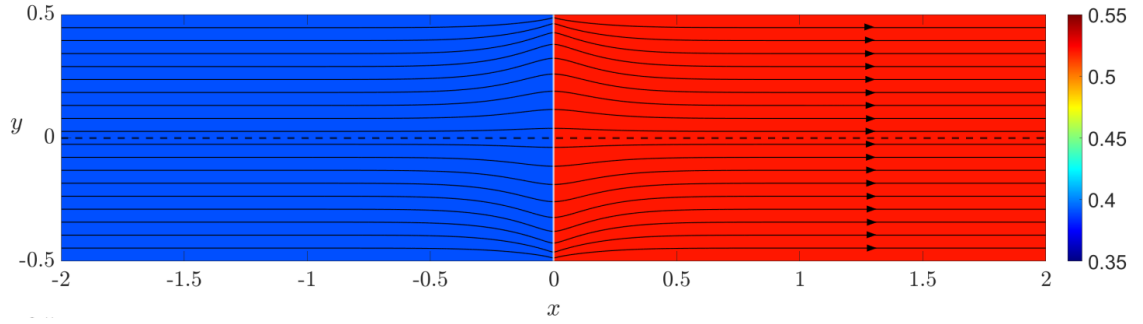

(b) Macroscopic model

Fig. 5.6: Isocontours of concentration with flow streamlines. (a) is the solution of the full-scale equation (3.4). (b) is the solution of the macroscopic model derived via homogenization, (3.17–3.20). The black lines represent the streamlines. In (a) the white circles are the solid inclusions forming the membrane. In (b) the vertical white line represents the equivalent macroscopic membrane.

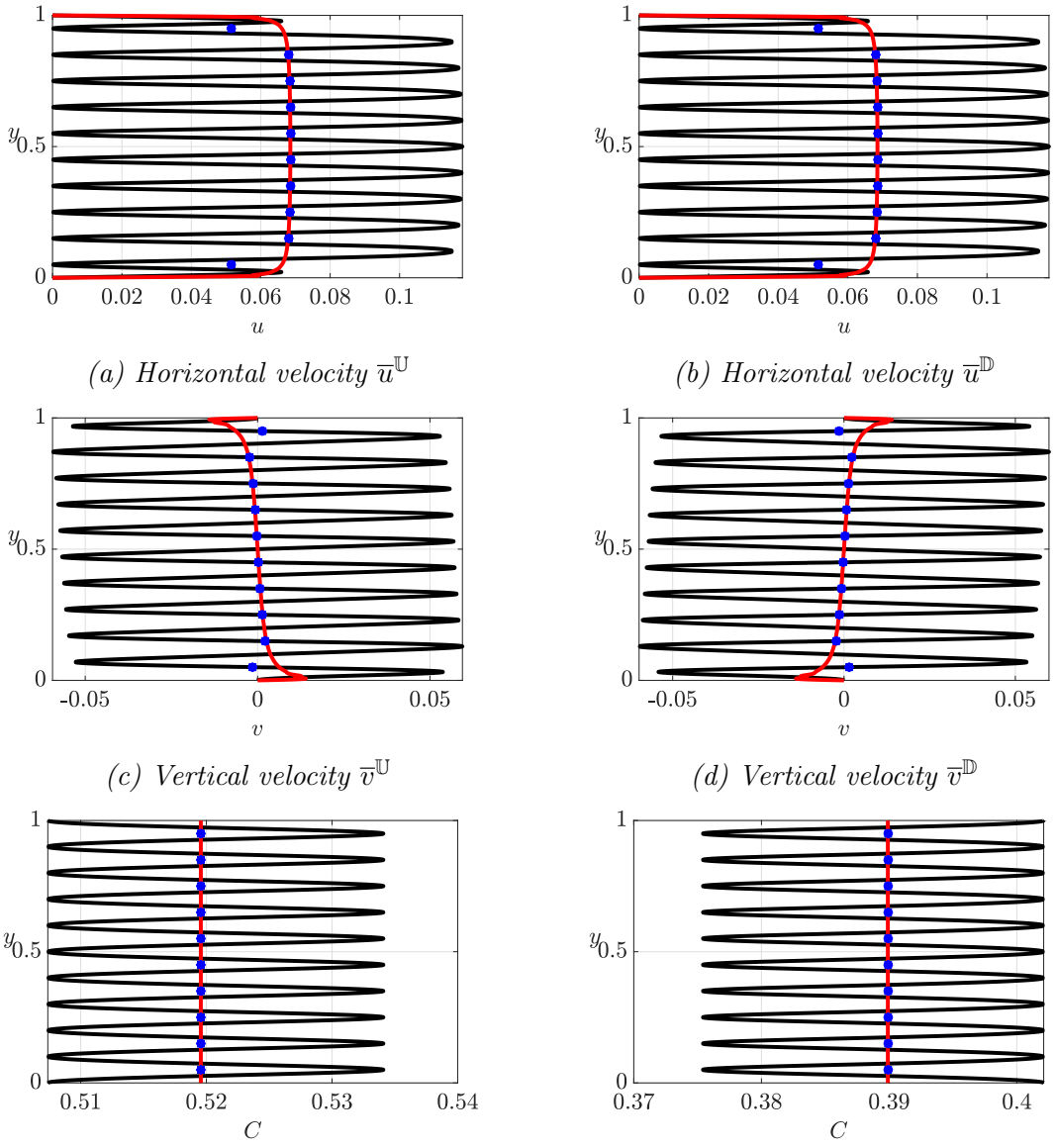

(a) Horizontal velocity $\overline{u}^{\mathbb{U}}$ *(b) Horizontal velocity* $\overline{u}^{\mathbb{D}}$

(c) Vertical velocity $\overline{v}^{\mathbb{U}}$ *(d) Vertical velocity* $\overline{v}^{\mathbb{D}}$

(e) Concentration $\overline{c}^{\mathbb{U}}$ *(f) Concentration* $\overline{c}^{\mathbb{D}}$

Fig. 5.7: Quantitative comparison for ε*=0.1. Horizontal velocities (a,b), vertical velocities (c,d) and concentrations (e,f) have been evaluated along the membrane. Frames (a,c,e) refer to* $\overline{\cdot}^{\mathbb{U}}$ *(3.16). Frames (b,d,f) refer to the* $\overline{\cdot}^{\mathbb{D}}$ *(3.16). Black profiles refer to the solution of full-scale equations (3.4). The solid red lines refer to the solution of the macroscopic model (3.17–3.20). The blue points represent the average of the full-scale solution.*

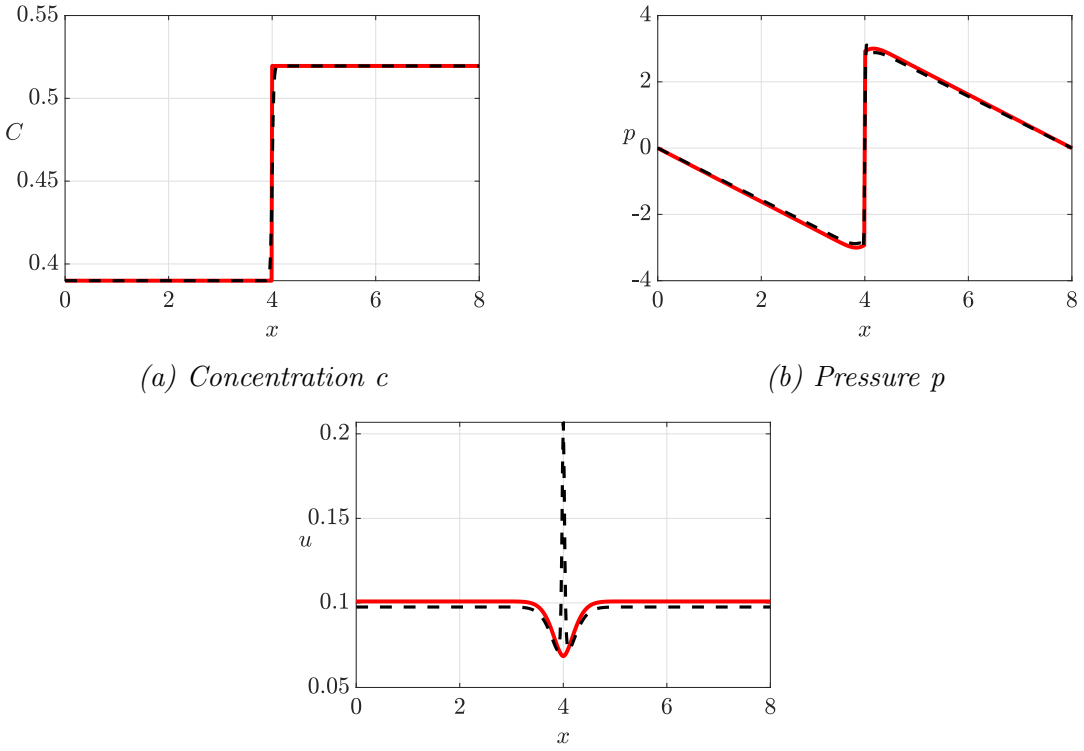

(a) Concentration c

(b) Pressure p

(c) Vertical velocity v

Fig. 5.8: Quantitative comparison for ε=0.1 over the center line of the channel (horizontal dashed line sketched in figure 5.1). Black profiles refer to the solution of the full-scale equation (3.4). The solid red line refer to the solution of the macroscopic model (3.17–3.20).

5.4 Validation Case 3

We changed the concentration imposed on the inclusion $\partial\mathbb{M}$, using equation (4.1) with $\theta = 45°$and $\theta = 315°$to specify the concentration on $\partial\mathbb{M}$.

For the case of $\theta = 45°$ a vertical positive velocity is generated as it can be seen in figure 5.9b while for $\theta = 315°$ the vertical velocity is negative (cf. figure 5.10b).

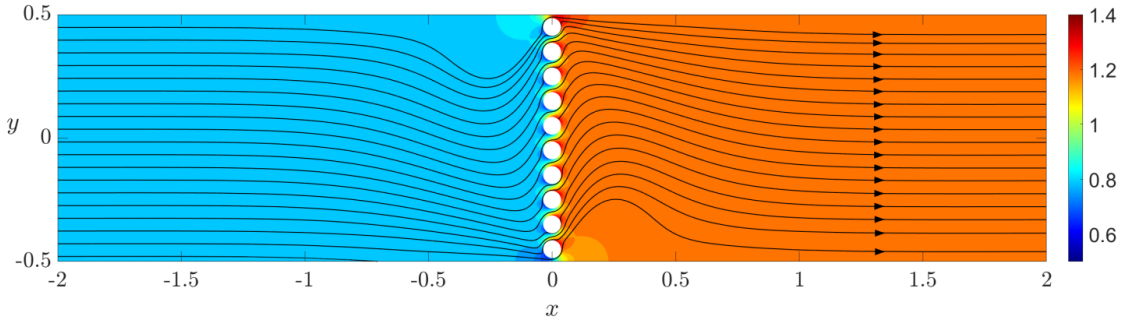

(a) DNS, $\theta = 45°$

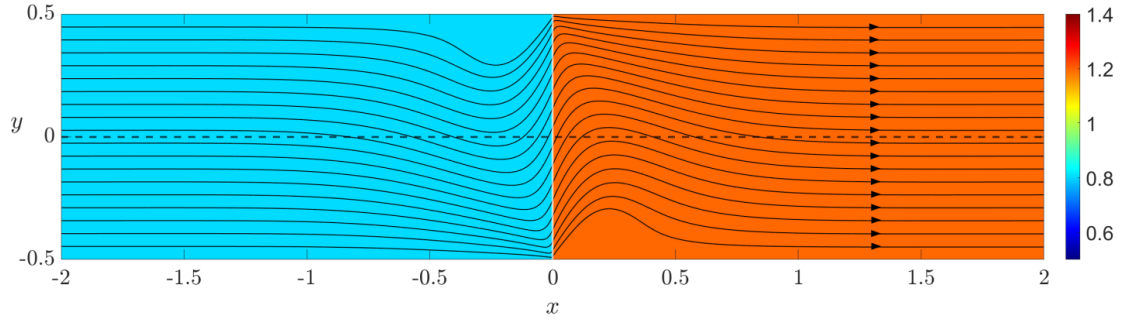

(b) Macro-model, $\theta = 45°$

Fig. 5.9: Isocontours of concentration with flow streamlines. (a) is the solution of the full-scale equation (3.4). (b) is the solution of the macroscopic model derived via homogenization (3.17–3.20). The black lines represent the streamlines. In (a) the white circles are the solid inclusions forming the membrane. In (b) the vertical white line represents the equivalent macroscopic membrane.

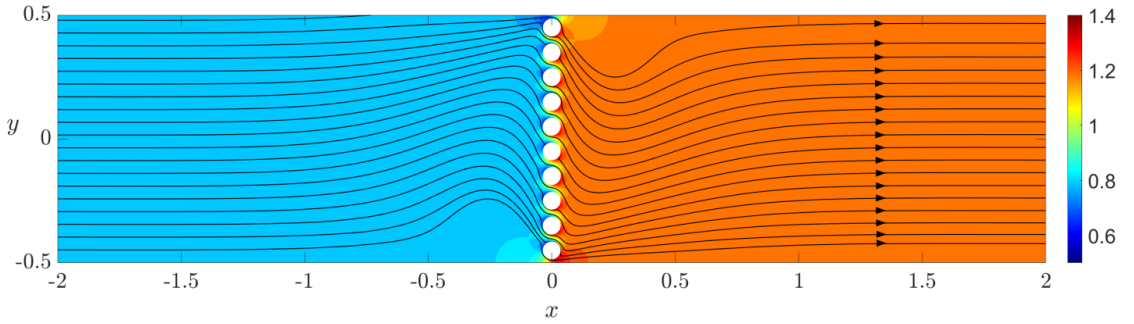

(a) DNS, $\theta = 315^\circ$

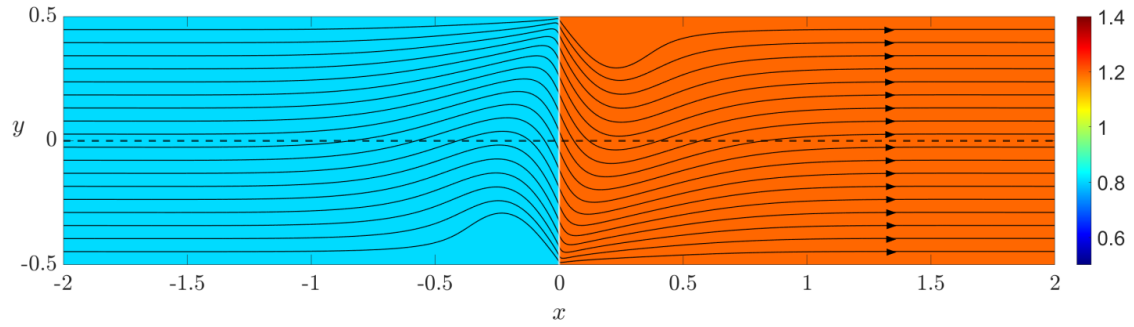

(b) Macro-model, $\theta = 315^\circ$

Fig. 5.10: Isocontours of concentration with flow streamlines. (a) is the solution of the full-scale equation (3.4). (b) is the solution of the macroscopic model derived via homogenization (3.17–3.20). The black lines represent the streamlines. In (a) the white circles are the solid inclusions forming the membrane. In (b) the vertical white line represents the equivalent macroscopic membrane.

Quantitative comparisons between the macroscopic solution and the DNS are shown in figures 5.11, 5.12 and 5.13.

$$\theta = 45^\circ$$

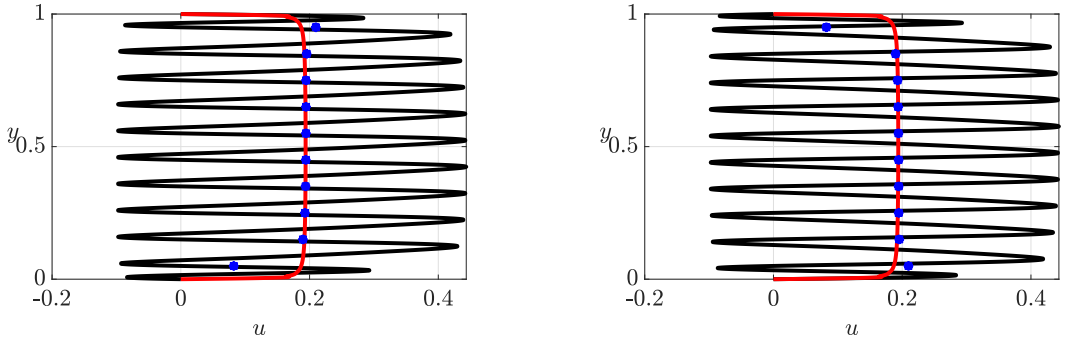

(a) Horizontal velocity $\overline{u}^{\mathbb{U}}$

(b) Horizontal velocity $\overline{u}^{\mathbb{D}}$

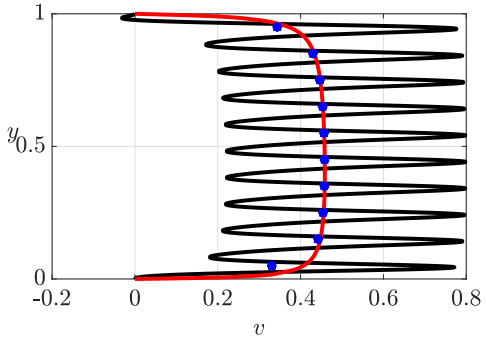

(c) Vertical velocity $\overline{v}^{\mathbb{U}}$

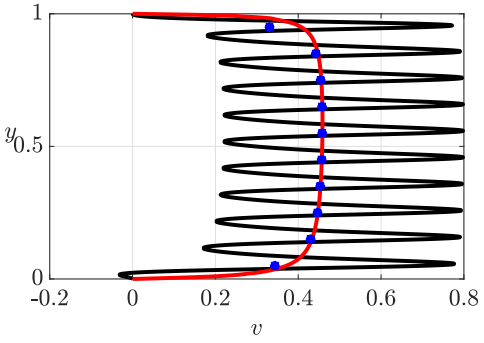

(d) Vertical velocity $\overline{v}^{\mathbb{D}}$

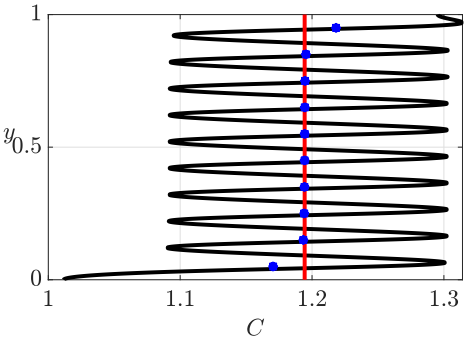

(e) Concentration $\overline{c}^{\mathbb{U}}$

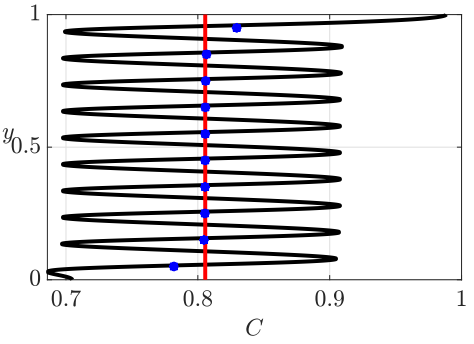

(f) Concentration $\overline{c}^{\mathbb{D}}$

Fig. 5.11: Quantitative comparison for ε=0.1. Horizontal velocities (a,b), vertical velocities (c,d) and concentrations (e,f) have been evaluated along the membrane. Frames (a,c,e) refer to $\overline{\cdot}^{\mathbb{U}}$ (3.16). Frames (b,d,f) refer to the $\overline{\cdot}^{\mathbb{D}}$ (3.16). Black profiles refer to the solution of full-scale equations (3.4). The solid red lines refer to the solution of the macroscopic model (3.17–3.20). The blue points represent the average of the full-scale solution.

$\theta = 315°$

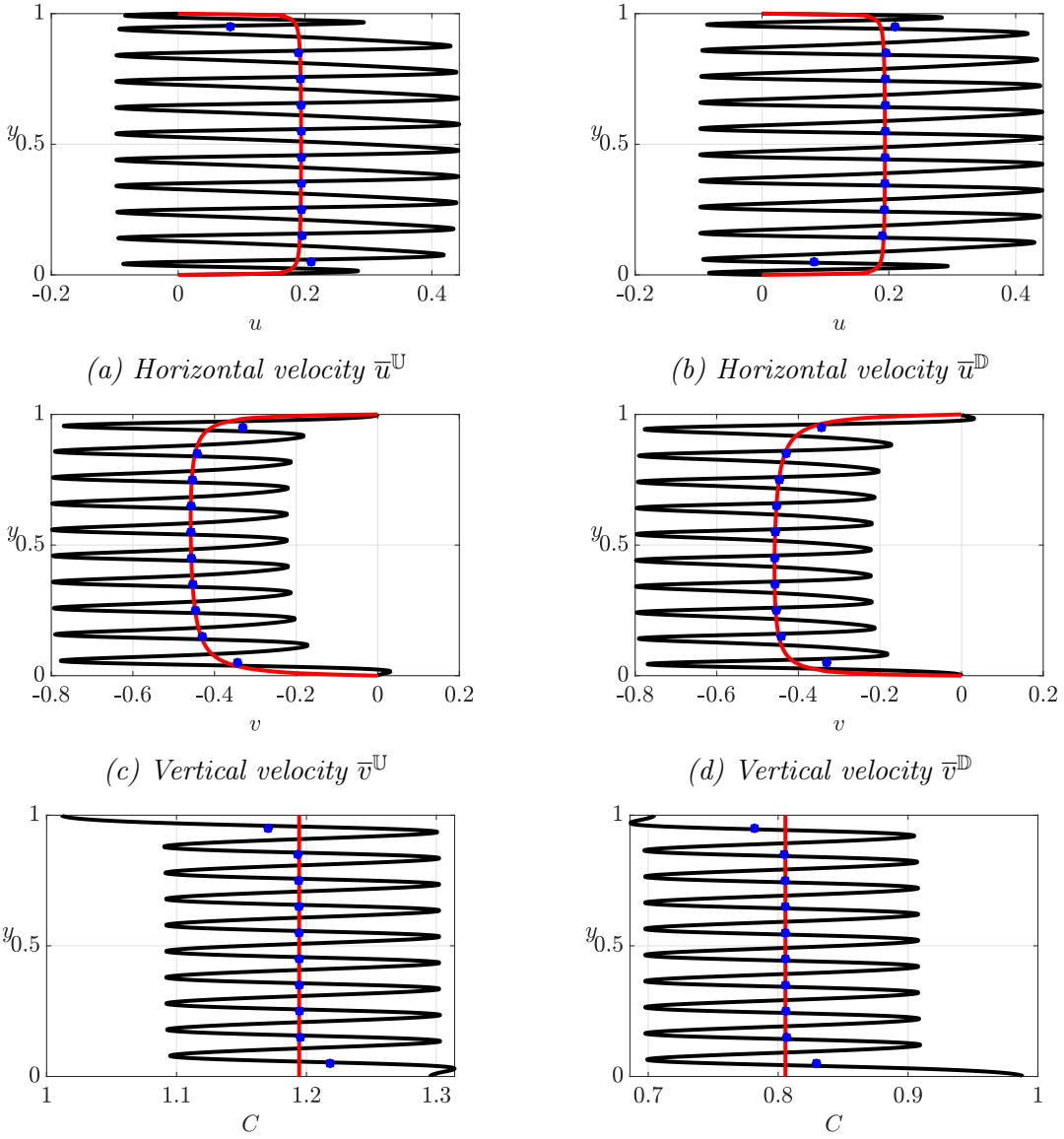

(a) Horizontal velocity $\overline{u}^{\mathbb{U}}$ *(b) Horizontal velocity* $\overline{u}^{\mathbb{D}}$

(c) Vertical velocity $\overline{v}^{\mathbb{U}}$ *(d) Vertical velocity* $\overline{v}^{\mathbb{D}}$

(e) Concentration $\overline{c}^{\mathbb{U}}$ *(f) Concentration* $\overline{u}^{\mathbb{D}}$

Fig. 5.12: Quantitative comparison for ε*=0.1. Horizontal velocities (a,b), vertical velocities (c,d) and concentrations (e,f) have been evaluated along the membrane. Frames (a,c,e) refer to* $\dot{\cdot}^{\mathbb{U}}$ *(3.16). Frames (b,d,f) refer to the* $\dot{\cdot}^{\mathbb{D}}$ *(3.16). Black profiles refer to the solution of full-scale equations (3.4). The solid red lines refer to the solution of the macroscopic model (3.17–3.20). The blue points represent the average of the full-scale solution.*

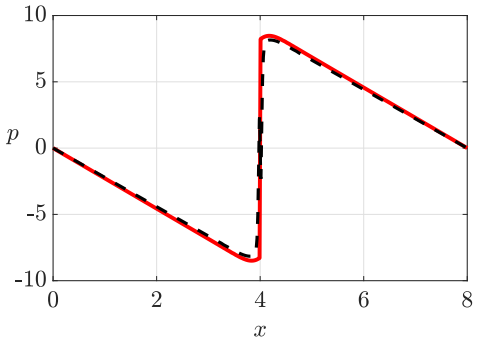

(a) Pressure $\theta = 45^\circ$

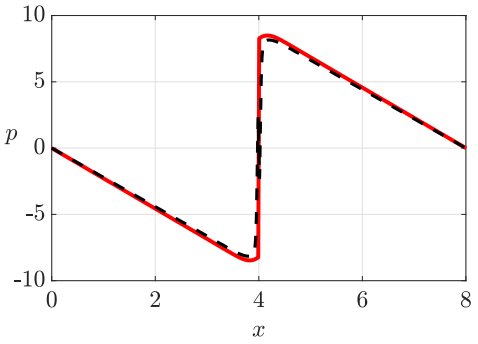

(b) Pressure $\theta = 315^\circ$

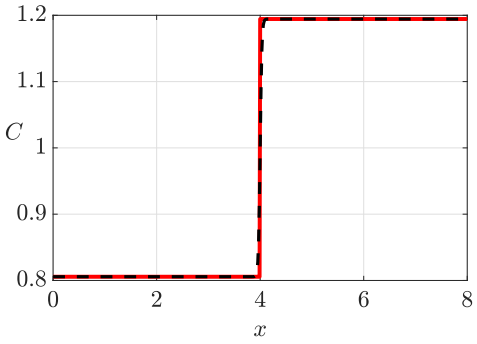

(c) Concentration $\theta = 45^\circ$

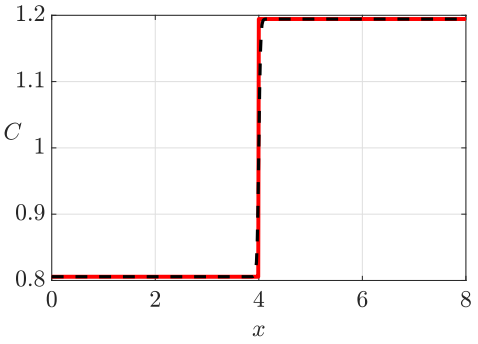

(d) Concentration $\theta = 315^\circ$

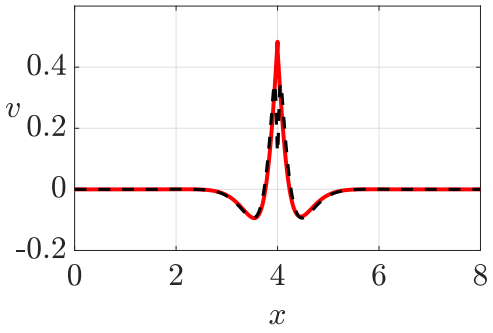

(e) Vertical velocity $\theta = 45^\circ$

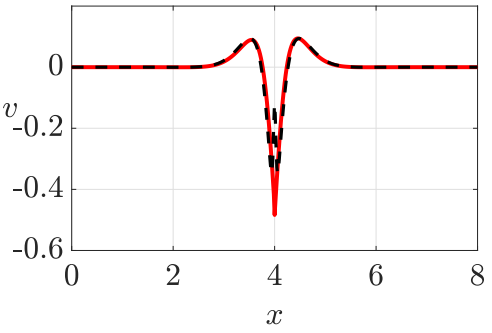

(f) Vertical velocity $\theta = 315^\circ$

Fig. 5.13: Quantitative comparison for ε=0.1 over the center line of the channel (horizontal dashed line sketched in figure 5.1). Black profiles refer to the solution of the full-scale equation (3.4). The solid red line refer to the solution of the macroscopic model (3.17–3.20).

5.5 Validation case 4

We consider a circular-shaped membrane placed in a 2D channel (cf. figure 5.1b). Varying θ in equation (4.1) along the cylinder, we generate several flow patterns. For the curvilinear coordinate of the membrane, the rear stagnation point with anti-clockwise direction was taken as a reference point.

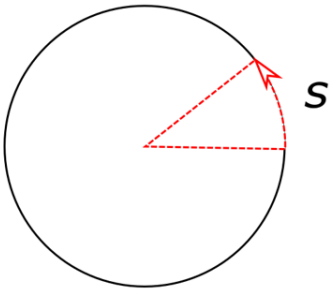

Fig. 5.14: Curvilinear coordinate s

5.5.1 Case 4.1

In this case, we create two different zones of recirculation. The conditions imposed on $\partial\mathbb{M}$ are $c = cos(0)n_x + sen(0)n_y + 1$ if $s \in [0, \frac{\pi}{4}]$ and $s \in [\pi, \frac{3\pi}{4}]$, in the other part c has a constant value equal to 0.

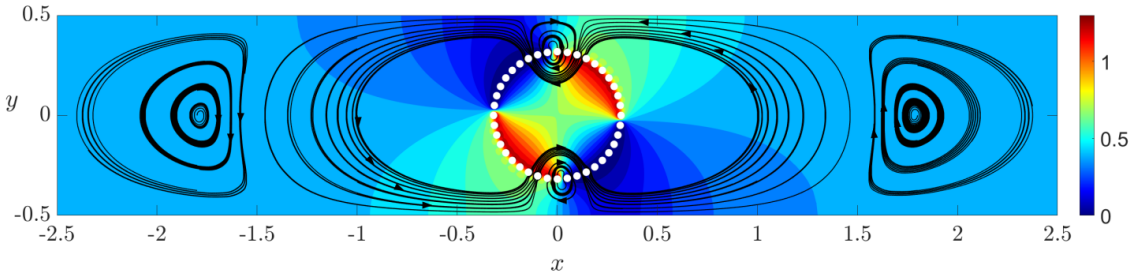

(a) DNS

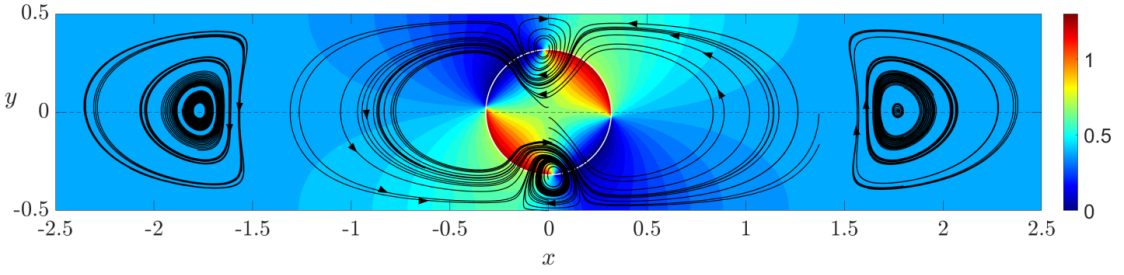

(b) Macro-model

Fig. 5.15: Isocontours of concentration with flow streamlines. (a) is the solution of the full-scale equation (3.4). (b) is the solution of the macroscopic model derived via homogenization (3.17–3.20). The black lines represent the streamlines. In (a) the white circles are the solid inclusions forming the membrane. In (b) the white cylinder represents the equivalent macroscopic membrane.

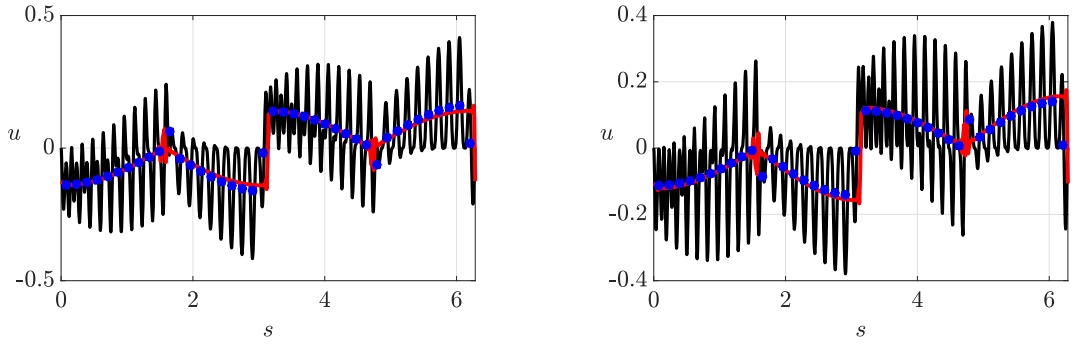

(a) Horizontal velocity $\overline{u}^{\mathbb{U}}$

(b) Horizontal velocity $\overline{u}^{\mathbb{D}}$

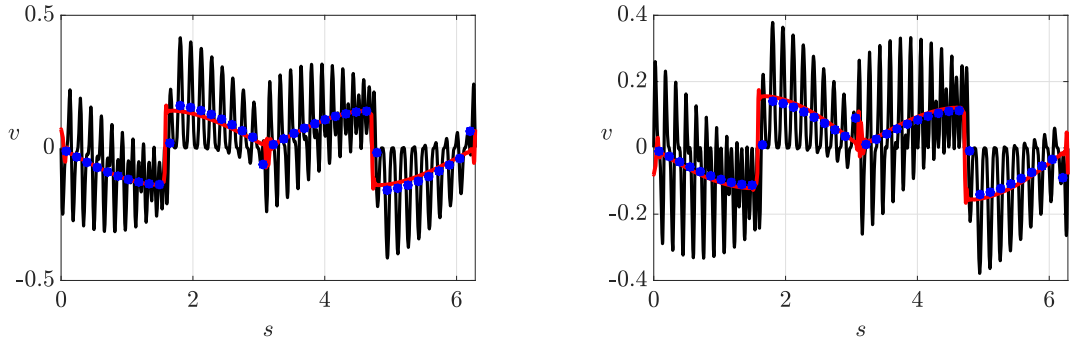

(c) Vertical velocity $\overline{v}^{\mathbb{U}}$

(d) Vertical velocity $\overline{v}^{\mathbb{D}}$

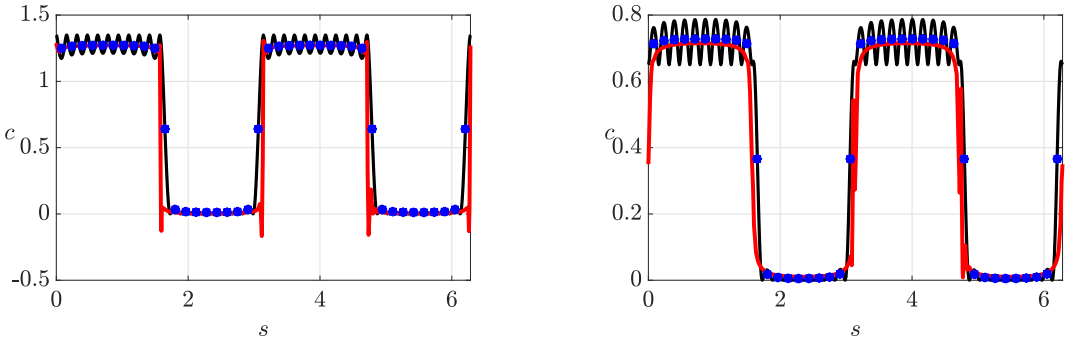

(e) Concentration $\overline{c}^{\mathbb{U}}$

(f) Concentration $\overline{c}^{\mathbb{D}}$

Fig. 5.16: Quantitative comparison for ε*=0.05. Horizontal velocities (a,b), vertical velocities (c,d) and concentrations (e,f) have been evaluated along the membrane. Frames (a,c,e) refer to* $\overline{\cdot}^{\mathbb{U}}$ *(3.16). Frames (b,d,f) refer to the* $\overline{\cdot}^{\mathbb{D}}$ *(3.16). Black profiles refer to the solution of full-scale equations (3.4). The solid red lines refer to the solution of the macroscopic model (3.17–3.20). The blue points represent the average of the full-scale solution.*

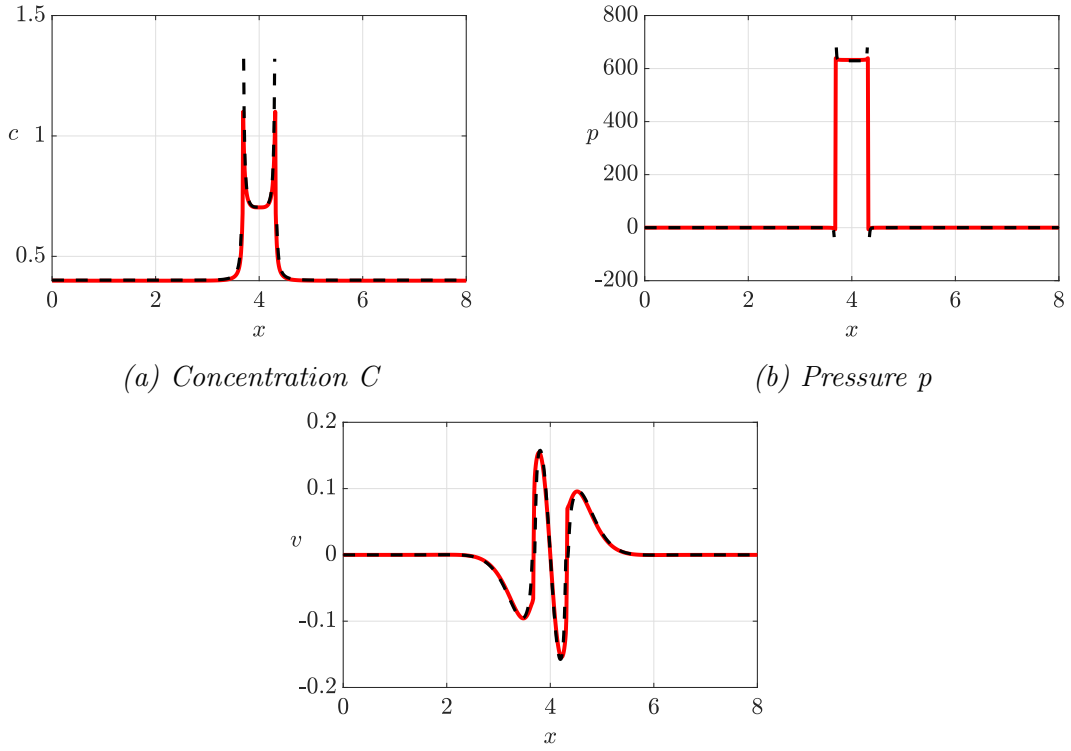

(a) Concentration C

(b) Pressure p

(c) Vertical velocity v

Fig. 5.17: Quantitative comparison for ε=0.05 over the center line of the channel (horizontal dashed line sketched in figure 5.1). Black profiles refer to the solution of the full-scale equation (3.4). The solid red line refer to the solution of the macroscopic model (3.17–3.20).

5.5.2 Case 4.2

The condition for c on $\partial\mathbb{M}$ is $c = cos(\frac{\pi}{2})n_x + sen(\frac{\pi}{2})n_y + 1$. Getting far from $\mathbb{C}$ the concentration has a constant value. The net flow rate along each vertical line is equal to zero.

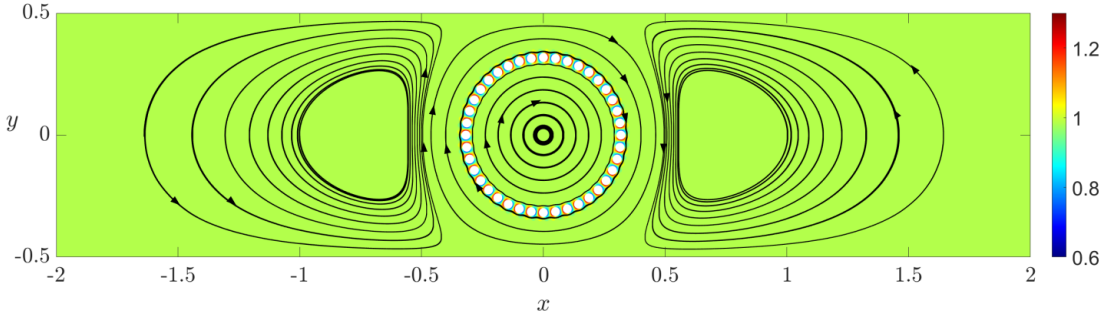

(a) DNS

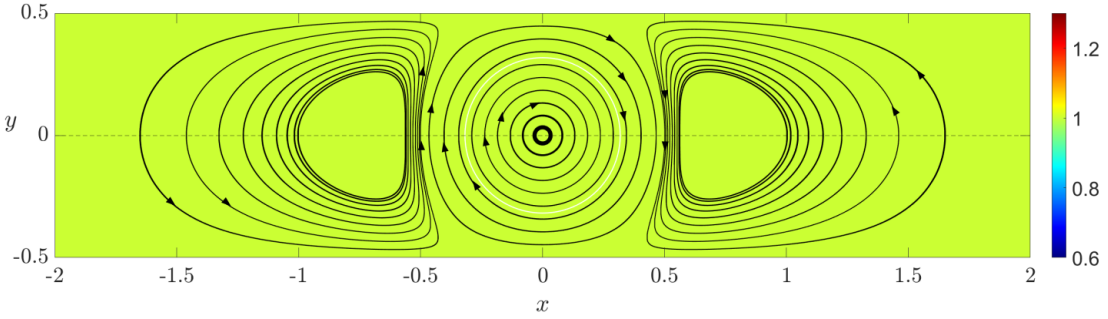

(b) Macro-model

Fig. 5.18: Isocontours of concentration with flow streamlines. (a) is the solution of the full-scale equation (3.4). (b) is the solution of the macroscopic model derived via homogenization (3.17–3.20). The black lines represent the streamlines. In (a) the white circles are the solid inclusions forming the membrane. In (b) the white cylinder represents the equivalent macroscopic membrane.

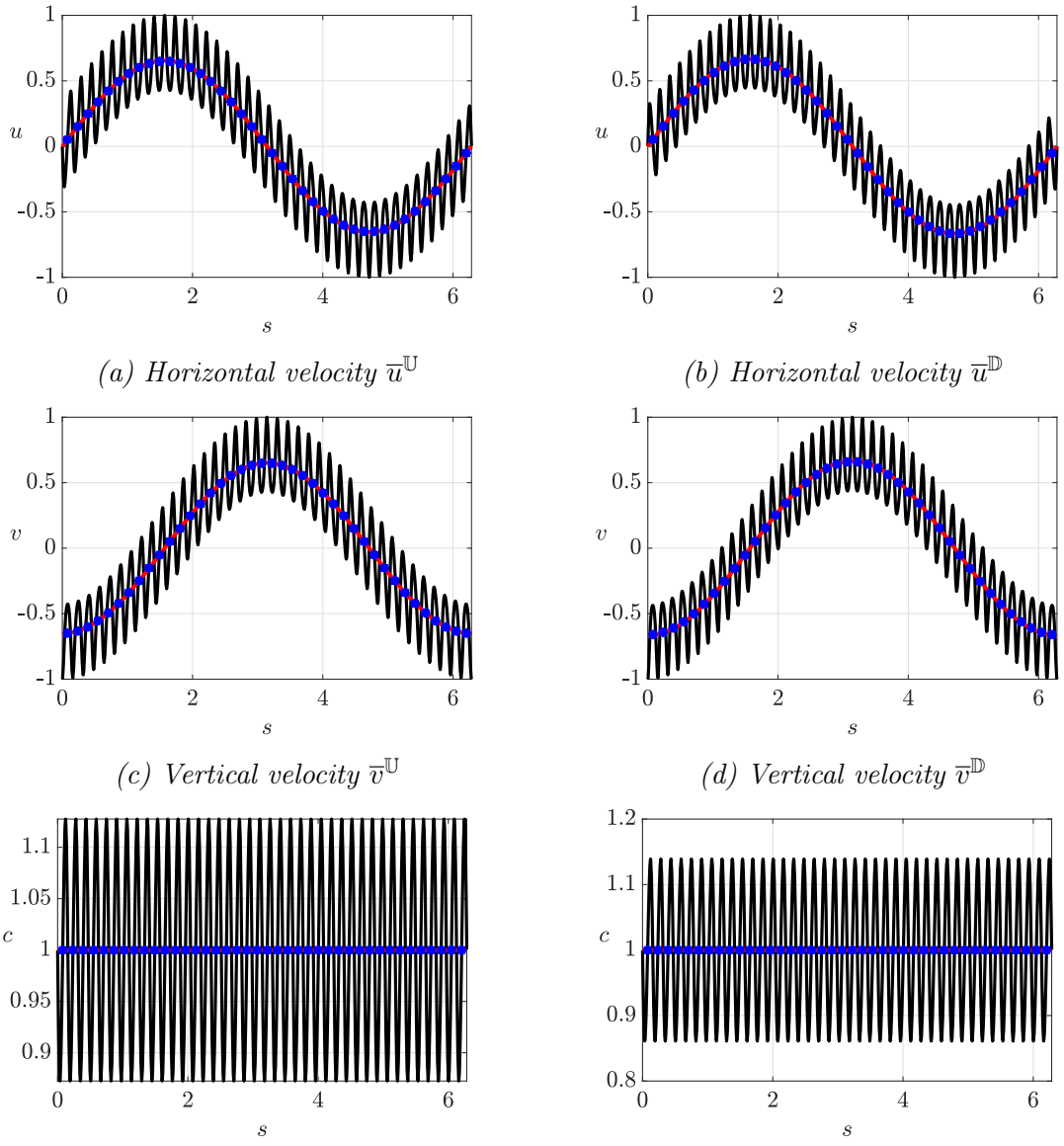

(a) Horizontal velocity $\overline{u}^{\mathbb{U}}$

(b) Horizontal velocity $\overline{u}^{\mathbb{D}}$

(c) Vertical velocity $\overline{v}^{\mathbb{U}}$

(d) Vertical velocity $\overline{v}^{\mathbb{D}}$

(e) Concentration $\overline{c}^{\mathbb{U}}$

(f) Concentration $\overline{c}^{\mathbb{D}}$

Fig. 5.19: Quantitative comparison for ε=0.05. Horizontal velocities (a,b), vertical velocities (c,d) and concentrations (e,f) have been evaluated along the membrane. Frames (a,c,e) refer to $\overline{\cdot}^{\mathbb{U}}$ (3.16). Frames (b,d,f) refer to the $\overline{\cdot}^{\mathbb{D}}$ (3.16). Black profiles refer to the solution of full-scale equations (3.4). The solid red lines refer to the solution of the macroscopic model (3.17–3.20). The blue points represent the average of the full-scale solution.

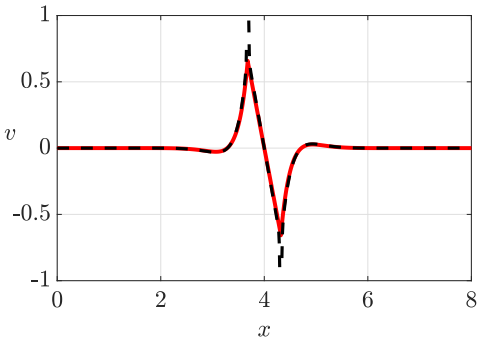

(a) Vertical velocity v

Fig. 5.20: Quantitative comparison for the vertical velocity for ε=0.05 over the center line of the channel (horizontal dashed line sketched in figure 5.1). Black profiles refer to the solution of the full-scale equation (3.4). The solid red line refer to the solution of the macroscopic model (3.17–3.20).

5.5.3 Case 4.3

The condition for c on $\partial\mathbb{M}$ is $c = cos(\pi)n_x + sen(\pi)n_y + 1$ if $s \in [-\frac{\pi}{4}, \frac{\pi}{4}]$, $c = cos(0)n_x + sen(0)n_y + 1$ if $s \in [\frac{3\pi}{4}, \frac{5\pi}{4}]$, in the remaining part of the cylinder c has a constant value equal to 0. As a result, two recirculation zones are created above and below the circular membrane. With this configuration we are able to create a net flow through the channel, pointing from left to right.

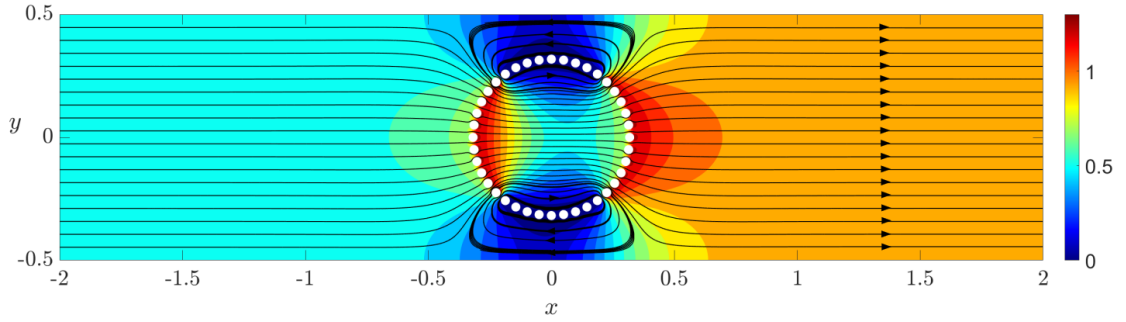

(a) DNS

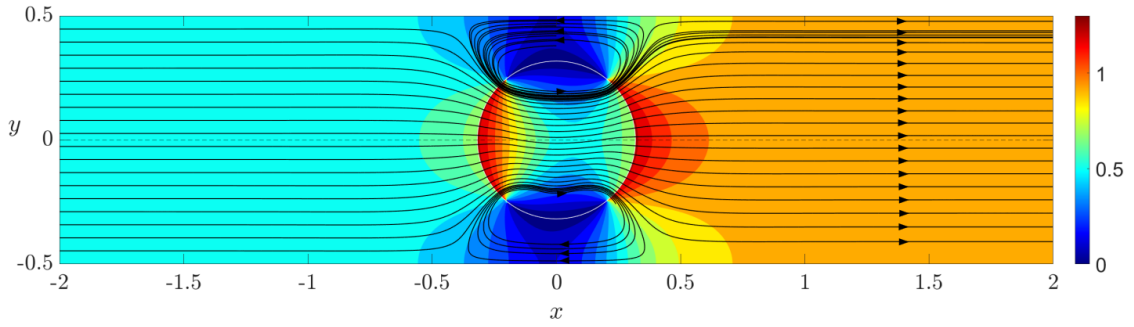

(b) Macroscopic model

Fig. 5.21: Isocontours of concentration with flow streamlines. (a) is the solution of the full-scale equation (3.4). (b) is the solution of the macroscopic model derived via homogenization (3.17–3.20). The black lines represent the streamlines. In (a) the white circles are the solid inclusions forming the membrane. In (b) the white cylinder represents the equivalent macroscopic membrane.

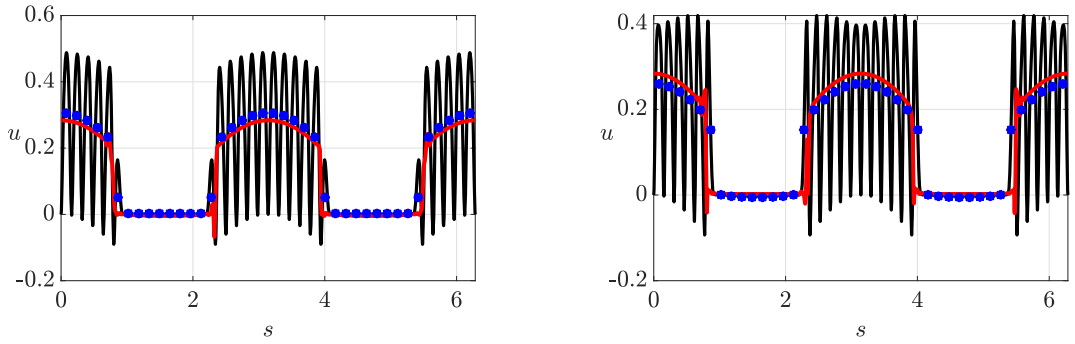

(a) Horizontal velocity $\overline{u}^{\mathbb{U}}$

(b) Horizontal velocity $\overline{u}^{\mathbb{D}}$

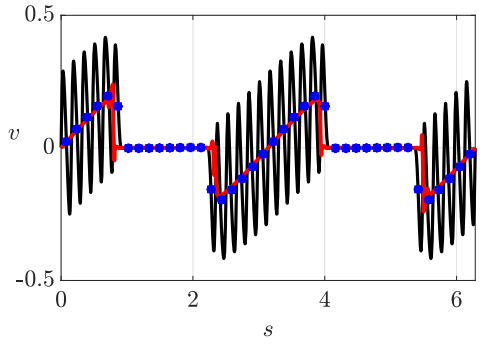

(c) Vertical velocity $\overline{v}^{\mathbb{U}}$

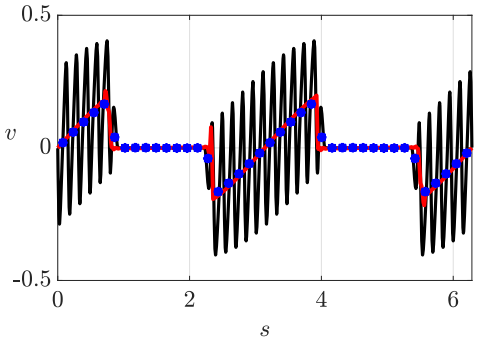

(d) Vertical velocity $\overline{v}^{\mathbb{D}}$

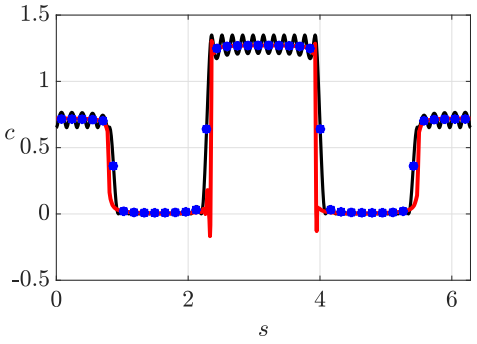

(e) Concentration $\overline{c}^{\mathbb{U}}$

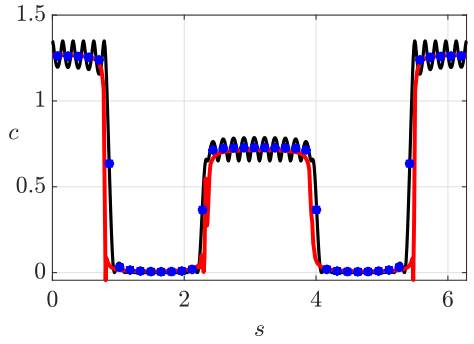

(f) Concentration $\overline{c}^{\mathbb{D}}$

Fig. 5.22: Quantitative comparison for ε=0.05. Horizontal velocities (a,b), vertical velocities (c,d) and concentrations (e,f) have been evaluated along the membrane. Frames (a,c,e) refer to $\overline{\cdot}^{\mathbb{U}}$ (3.16). Frames (b,d,f) refer to the $\overline{\cdot}^{\mathbb{D}}$ (3.16). Black profiles refer to the solution of full-scale equations (3.4). The solid red lines refer to the solution of the macroscopic model (3.17–3.20). The blue points represent the average of the full-scale solution.

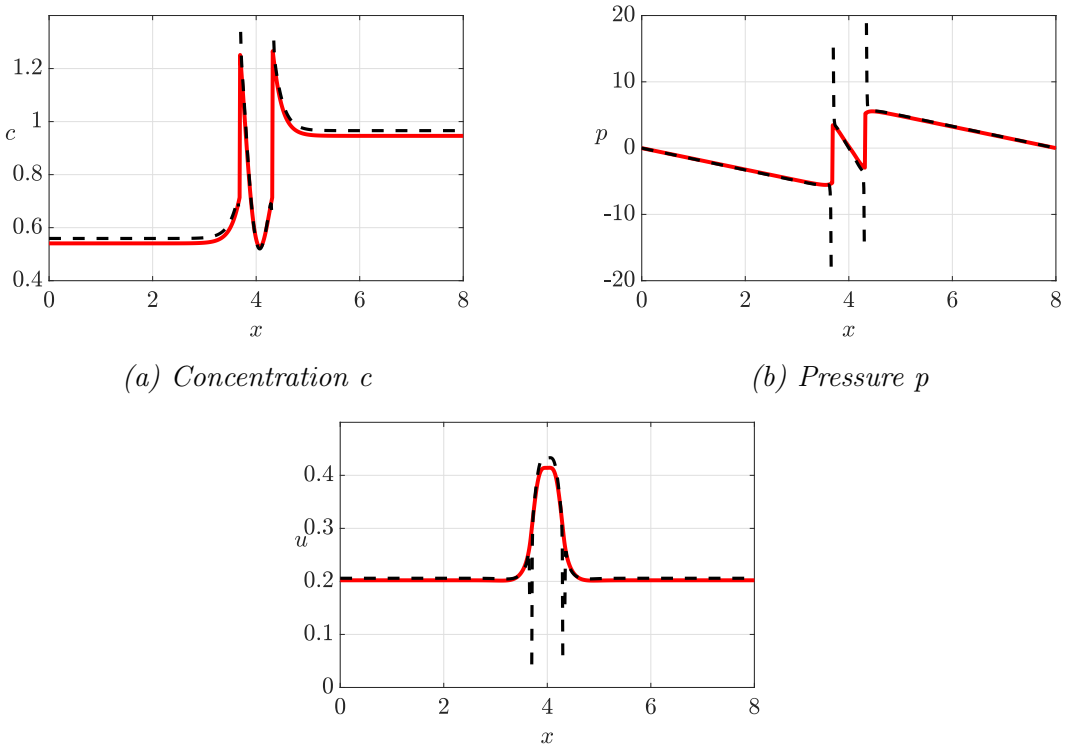

(a) Concentration c

(b) Pressure p

(c) Horizontal velocity u

Fig. 5.23: Quantitative comparison for ε=0.05 over the center line of the channel (horizontal dashed line sketched in figure 5.1. Black profiles refer to the solution of the full-scale equation (3.4). The solid red line refer to the solution of the macroscopic model (3.17–3.20).

5.6 Validation Case 5

The solutions presented in the previous chapter are carried out for $Pe^{\mathbb{O}} = 0$. We now analyse the reliability of the model with positive $Pe^{\mathbb{O}}$ for the configuration presented in section 5.2.

The relative error is defined as the difference on the macroscopic membrane between the average concentration calculated from the DNS, $\overline{C}$, and the concentration calculated with the macroscopic model, c, on the central point of the membrane ($x = \frac{L_x}{2}$ and $y = \frac{L_y}{2}$) i.e

$$e = \frac{\mid \overline{C} - c \mid}{\frac{\overline{C}+c}{2}}. \tag{5.2}$$

Errors below ε are noticed for values of $Pe^{\mathbb{O}}$ up to ε^{-2}, in agreement with the precision predicted by the homogenization theory.

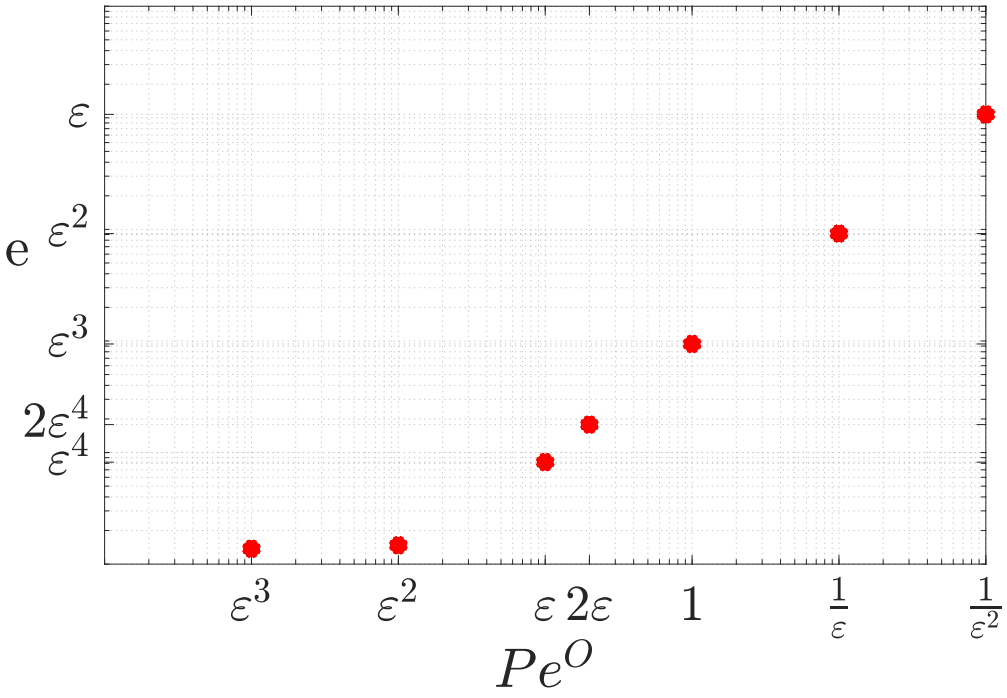

Fig. 5.24: Relative error for the concentration on the membrane.

6 Homogenization of the long range potential equations

We now consider the case introduced in section 2.3 where the range of action of the potential ϕ is comparable with the pore size, i.e $\delta \approx 1$. We perform homogenization of the following set of equations

$$\begin{cases} \rho\hat{\partial}_t u_i + \rho\hat{u}_j\hat{\partial}_j u_i = -\hat{\partial}_i\hat{p} + \mu\hat{\partial}^2_{ll}\hat{u}_i - \hat{c}\hat{\partial}_i k_b T\phi \\ \hat{\partial}_i\hat{u}_i = 0 \\ \partial_{\hat{t}}\hat{c} + \hat{\partial}_i\hat{F}_i = 0 \\ \hat{F}_i = \hat{u}_i\hat{c} - D(\hat{\partial}_i\hat{c} + \hat{c}\hat{\partial}_i\phi) \\ \hat{u}^s_i = 0 \text{ on } \partial\mathbb{M} \\ \hat{F}_i n^{\mathbb{M}}_i = A(x) \text{ on } \partial\mathbb{M} \end{cases} \tag{6.1}$$

The last two equations are the boundary conditions on the solid inclusions $\partial\mathbb{M}$.

6.1 Homogenization procedure

For the inner problem valid within the domain sketched in figure 3.1, whose variables are denoted with the superscript $\mathbb{I}$, we use the following normalization

$$c^* = \Delta C^{\mathbb{I}} c^{\mathbb{I}} \ , \quad \hat{x} = l x^{\mathbb{I}} \ , \quad \hat{p} = k_b T \Delta C^{\mathbb{I}} p^{\mathbb{I}} \ , \quad \hat{u} = U^{\mathbb{I}} u^{\mathbb{I}} = \frac{l k_b T \Delta C^{\mathbb{I}}}{\mu}\mathbf{u}^{\mathbb{I}}. \tag{6.2}$$

The dimensionless equations are

$$\begin{cases} Re_l u^{\mathbb{I}}_j \partial_j u^{\mathbb{I}}_i = -\partial_i p^{\mathbb{I}} + \partial^2_{ll} u^{\mathbb{I}}_i - c^{\mathbb{I}}\partial_i\phi \\ \partial_i u^{\mathbb{I}}_i = 0 \\ \partial_i F^{\mathbb{I}}_i = 0 \\ F^{\mathbb{I}}_i = Pe^{\mathbb{I}} u^{\mathbb{I}}_i c^{\mathbb{I}} - D(\partial_i c^{\mathbb{I}} + c^{\mathbb{I}}\partial_i\phi) \\ u^s_i = 0 \text{ on } \partial\mathbb{M} \\ F_i n^{\mathbb{M}}_i = A(x) \text{ on } \partial\mathbb{M}. \end{cases} \tag{6.3}$$

Following the procedure introduced in chapter 3, the unknown variables are decomposed as in equations (3.5), while the spatial derivatives are transformed following rule (3.6). The leading order approximation of equations (6.3) reads

$$\begin{cases} Re_l u^{\mathbb{I},0}_j \partial_j u^{\mathbb{I},0}_i = -\partial_i p^{\mathbb{I},0} + \partial^2_{ll} u^{\mathbb{I},0}_i - \frac{\Delta c^{\mathbb{I},0} k_b T}{\Delta p} c^{\mathbb{I},0}\partial_i\phi \\ \partial_i u^{\mathbb{I},0}_i = 0 \\ \partial_i F^{\mathbb{I},0}_i = 0 \\ F^{\mathbb{I},0}_i = Pe^{\mathbb{I},0} u^{\mathbb{I},0}_i c^{\mathbb{I},0} - D(\partial_i c^{\mathbb{I},0} + c^{\mathbb{I},0}\partial_i\phi) \\ u^s_i = 0 \text{ on } \partial\mathbb{M} \\ F^{\mathbb{I},0}_i n^{\mathbb{M}}_i = A(x) \text{ on } \partial\mathbb{M}. \end{cases} \tag{6.4}$$

Re_l and $Pe^{\mathbb{I}}$ are assumed of order ε and problem (6.4) is reduced to

$$\begin{cases} -\partial_i p^{\mathbb{I},0} + \partial^2_{ll} u_i^{\mathbb{I},0} - c^{\mathbb{I},0}\partial_i \phi = 0 \\ \partial_i u_i^{\mathbb{I},0} = 0 \\ \partial_i F_i^{\mathbb{I},0} = 0 \\ F_i^{\mathbb{I},0} = -D(\partial_i c^{\mathbb{I},0} + c^{\mathbb{I},0}\partial_i \phi) \\ u_i^s = 0 \ \text{ on } \partial\mathbb{M} \\ F_i^{\mathbb{I},0} n_i^{\mathbb{M}} = A(x) \ \text{ on } \partial\mathbb{M}. \end{cases} \tag{6.5}$$

On $\mathbb{U}$ and $\mathbb{D}$ boundary conditions in equations (3.9) and (3.10) hold.

6.1.1 Microscopic problem

Since the problem is linear, we can write the solution of equations (6.4) and (3.9) as

$$u_i^{\mathbb{I},0} = M_{ijk}\Sigma_{jk}^{\mathbb{O},\mathbb{U}} + N_{ijk}\Sigma_{jk}^{\mathbb{O},\mathbb{D}} + A_{ijk}F_i^{\mathbb{O},\mathbb{U}} + B_{ijk}F_i^{\mathbb{O},\mathbb{D}} + a_i \tag{6.6}$$

$$p^{\mathbb{I},0} = Q_{jk}\Sigma_{jk}^{\mathbb{O},\mathbb{U}} + R_{jk}\Sigma_{jk}^{\mathbb{O},\mathbb{D}} + C_{ijk}F_i^{\mathbb{O},\mathbb{U}} + D_{ijk}F_i^{\mathbb{O},\mathbb{D}} + \eta \tag{6.7}$$

$$c^{\mathbb{I},0} = T_i F_i^{\mathbb{O},\mathbb{U}} + Y_i F_i^{\mathbb{O},\mathbb{D}} + \gamma \tag{6.8}$$

where $\mathbf{M}$, $\mathbf{N}$, $\mathbf{A}$, $\mathbf{B}$, $\mathbf{C}$, $\mathbf{D}$, $\mathbf{Q}$, $\mathbf{R}$, $\mathbf{T}$ and $\mathbf{Y}$ are unknown tensors and vectors. γ is the phoretic contribution to $c^{\mathbb{I},0}$ which generates the phoretic velocity a_i. Equations (6.6) (6.7) and (6.8) are substituted into the leading order problem (6.4) and boundary condition (3.9), leading to the following systems of equations that can be solved within the microscopic domain for $\mathbf{M}$, $\mathbf{N}$, $\mathbf{A}$, $\mathbf{B}$, $\mathbf{C}$, $\mathbf{D}$, $\mathbf{Q}$, $\mathbf{R}$, $\mathbf{T}$, $\mathbf{Y}$, γ, a_i and δ,

$$\begin{cases} \partial^2_{ii} T_j + \partial_i\phi\partial_i T_j + T_j\partial^2_{ii}\phi = 0 \,\text{in } \mathbb{F} \\ (\partial_i T_j + T_j\partial_i\phi)n_i^{\mathbb{M}} = 0 \,\text{on } \partial\mathbb{M} \\ -\partial_i T_j n_i = n_j \,\text{on } \mathbb{U} \\ -\partial_i T_j n_i = 0 \,\text{on } \mathbb{D} \\ T_j \text{ periodic along } \hat{t} \text{ and } \hat{s} \end{cases} \qquad \begin{cases} \partial^2_{ii} Y_j + \partial_i\phi\partial_i Y_j + Y_j\partial^2_{ii}\phi = 0 \,\text{in } \mathbb{F} \\ (\partial_i Y_j + Y_j\partial_i\phi)n_i^{\mathbb{M}} = 0 \,\text{on } \partial\mathbb{M} \\ -\partial_i Y_j n_i = 0 \,\text{on } \mathbb{U} \\ -\partial_i Y_j n_i = n_j \,\text{on } \mathbb{D} \\ Y_j \text{ periodic along } \hat{t} \text{ and } \hat{s} \end{cases} \tag{6.9}$$

$$\begin{cases} \partial^2_{ii}\gamma + \partial_i\phi\partial_i\gamma + \gamma\partial^2_{ii}\phi = 0 \,\text{in } \mathbb{F} \\ (\partial_i\gamma + \gamma\partial_i\phi)n_i^{\mathbb{M}} = A(x) \,\text{on } \partial\mathbb{M} \\ -\partial_i\gamma n_i = 0 \,\text{on } \mathbb{U} \\ -\partial_i\gamma n_i = 0 \,\text{on } \mathbb{D} \end{cases} \tag{6.10}$$

$$\begin{cases} -\partial_i Q_{jk} + \partial^2_{ll} M_{ijk} = 0 \,\text{in } \mathbb{F} \\ \partial_i M_{ijk} = 0 \,\text{in } \mathbb{F} \\ M_{ijk} = 0 \,\text{on } \partial\mathbb{M} \\ \sum_{pq}(M_{\cdot jk}, Q_{jk})n_q = \delta_{jp}\delta_{kq}n_q \,\text{on } \mathbb{U} \\ \sum_{pq}(M_{\cdot jk}, Q_{jk})n_q = 0 \,\text{on } \mathbb{D} \\ M_{ijk}, Q_{jk} \text{ periodic along } \hat{t} \text{ and } \hat{s} \end{cases} \qquad \begin{cases} -\partial_i R_{jk} + \partial^2_{ll} N_{ijk} = 0 \,\text{in } \mathbb{F} \\ \partial_i N_{ijk} = 0 \,\text{in } \mathbb{F} \\ N_{ijk} = 0 \,\text{on } \partial\mathbb{M} \\ \sum_{pq}(N_{\cdot jk}, R_{jk})n_q = 0 \,\text{on } \mathbb{U} \\ \sum_{pq}(N_{\cdot jk}, R_{jk})n_q = \delta_{jp}\delta_{kq}n_q \,\text{on } \mathbb{D} \\ N_{ijk}, R_{jk} \text{ periodic along } \hat{t} \text{ and } \hat{s} \end{cases} \tag{6.11}$$

$$\begin{cases} -\partial_i C_{jk} + \partial^2_{ll} A_{ijk} + T_i \partial_i \phi = 0 \text{ in } \mathbb{F} \\ \partial_i A_{ijk} = 0 \text{ in } \mathbb{F} \\ A_{ijk} = 0 \text{ on } \partial\mathbb{M} \\ \sum_{pq} (A_{.jk}, C_{jk}) n_q = 0 \text{ on } \mathbb{U} \\ \sum_{pq} (A_{.jk}, C_{jk}) n_q = 0 \text{ on } \mathbb{D} \\ A_{ijk}, C_{jk} \text{ periodic along } \hat{t} \text{ and } \hat{s} \end{cases} \quad \begin{cases} -\partial_i D_{jk} + \partial^2_{ll} B_{ijk} + Y_i \partial_i \phi = 0 \text{ in } \mathbb{F} \\ \partial_i B_{ijk} = 0 \text{ in } \mathbb{F} \\ B_{ijk} = 0 \text{ on } \partial\mathbb{M} \\ \sum_{pq} (B_{.jk}, D_{jk}) n_q = 0 \text{ on } \mathbb{U} \\ \sum_{pq} (B_{.jk}, D_{jk}) n_q = 0 \text{ on } \mathbb{D} \\ B_{ijk}, D_{jk} \text{ periodic along } \hat{t} \text{ and } \hat{s} \end{cases} \tag{6.12}$$

$$\begin{cases} -\partial_i \eta_{jk} + \partial^2_{ll} a_i + \gamma \partial_i \phi = 0 \text{ in } \mathbb{F} \\ \partial_i a_i = 0 \text{ in } \mathbb{F} \\ a_i = 0 \text{ on } \partial\mathbb{M} \\ \sum_{pq} (a_., \eta_{jk}) n_q = 0 \text{ on } \mathbb{U} \\ \sum_{pq} (a_., \eta_{jk}) n_q = 0 \text{ on } \mathbb{D} \\ a_i, \eta_{jk} \text{ periodic along } \hat{t} \text{ and } \hat{s}. \end{cases} \tag{6.13}$$

6.1.2 From the microscopic solution to the macroscopic interface condition

Applying averages (3.16) to (6.6) and (6.8), we obtain

$$\overline{u}_i^{\mathbb{C}^-} = \overline{u}_i^{\mathbb{U}} = \overline{M}_{ijk}^{\mathbb{U}} \Sigma_{jk}^{\mathbb{C}^-} + \overline{N}_{ijk}^{\mathbb{U}} \Sigma_{jk}^{\mathbb{C}^+} + \overline{A}_{ijk}^{\mathbb{U}} F_{jk}^{\mathbb{C}^-} + \overline{B}_{ijk}^{\mathbb{U}} F_{jk}^{\mathbb{C}^+} + \overline{a}_i^{\mathbb{U}} \tag{6.14}$$

$$\overline{u}_i^{\mathbb{C}^+} = \overline{u}_i^{\mathbb{D}} = \overline{M}_{ijk}^{\mathbb{D}} \Sigma_{jk}^{\mathbb{C}^-} + \overline{N}_{ijk}^{\mathbb{D}} \Sigma_{jk}^{\mathbb{C}^+} + \overline{A}_{ijk}^{\mathbb{D}} F_{jk}^{\mathbb{C}^-} + \overline{B}_{ijk}^{\mathbb{D}} F_{jk}^{\mathbb{C}^+} + \overline{a}_i^{\mathbb{D}} \tag{6.15}$$

$$\overline{c}^{\mathbb{C}^-} = \overline{c}^{\mathbb{U}} = \overline{T}_i^{\mathbb{U}} F_i^{\mathbb{C}^-} + \overline{Y}_i^{\mathbb{U}} F_i^{\mathbb{C}^+} + \overline{\gamma}^{\mathbb{U}} \tag{6.16}$$

$$\overline{c}^{\mathbb{C}^+} = \overline{c}^{\mathbb{D}} = \overline{T}_i^{\mathbb{D}} F_i^{\mathbb{C}^-} + \overline{Y}_i^{\mathbb{D}} F_i^{\mathbb{C}^+} + \overline{\gamma}^{\mathbb{U}} \tag{6.17}$$

The macroscopic interface condition can be written using the outer scale (3.2) leading to

$$\overline{u}_i^{\mathbb{C}^-} = \overline{u}_i^{\mathbb{U}} = \varepsilon(\overline{M}_{ijk}^{\mathbb{U}} \Sigma_{jk}^{\mathbb{C}^-} + \overline{N}_{ijk}^{\mathbb{U}} \Sigma_{jk}^{\mathbb{C}^+} + \varepsilon \overline{A}_{ijk}^{\mathbb{U}} F_{jk}^{\mathbb{C}^-} + \varepsilon \overline{B}_{ijk}^{\mathbb{U}} F_{jk}^{\mathbb{C}^+} + \varepsilon \overline{a}_i^{\mathbb{U}}) \tag{6.18}$$

$$\overline{u}_i^{\mathbb{C}^+} = \overline{u}_i^{\mathbb{D}} = \varepsilon(\overline{M}_{ijk}^{\mathbb{D}} \Sigma_{jk}^{\mathbb{C}^-} + \overline{N}_{ijk}^{\mathbb{D}} \Sigma_{jk}^{\mathbb{C}^+} + \varepsilon \overline{A}_{ijk}^{\mathbb{D}} F_{jk}^{\mathbb{C}^-} + \varepsilon \overline{B}_{ijk}^{\mathbb{D}} F_{jk}^{\mathbb{C}^+} + \varepsilon \overline{a}_i^{\mathbb{D}}) \tag{6.19}$$

$$\overline{c}^{\mathbb{C}^-} = \overline{c}^{\mathbb{U}} = \varepsilon(\overline{T}_i^{\mathbb{U}} F_i^{\mathbb{C}^-} + \overline{Y}_i^{\mathbb{U}} F_i^{\mathbb{C}^+} + \gamma) \tag{6.20}$$

$$\overline{c}^{\mathbb{C}^+} = \overline{c}^{\mathbb{D}} = \varepsilon(\overline{T}_i^{\mathbb{D}} F_i^{\mathbb{C}^-} + \overline{Y}_i^{\mathbb{D}} F_i^{\mathbb{C}^+} + \gamma). \tag{6.21}$$

7 Long range potential: Microscopic solution

We present here the solution of the microscopic problems (6.9–6.13).
Following [20], the potential ϕ is defined as

$$\phi(x) = \frac{A}{2}(1 - tanh(\frac{d(x) - a}{\delta})) \tag{7.1}$$

where d(x) is the distance function from the center of the inclusion. The shape of the potential change with δ . In our case $A = 10$ and $\delta = 0.06$.

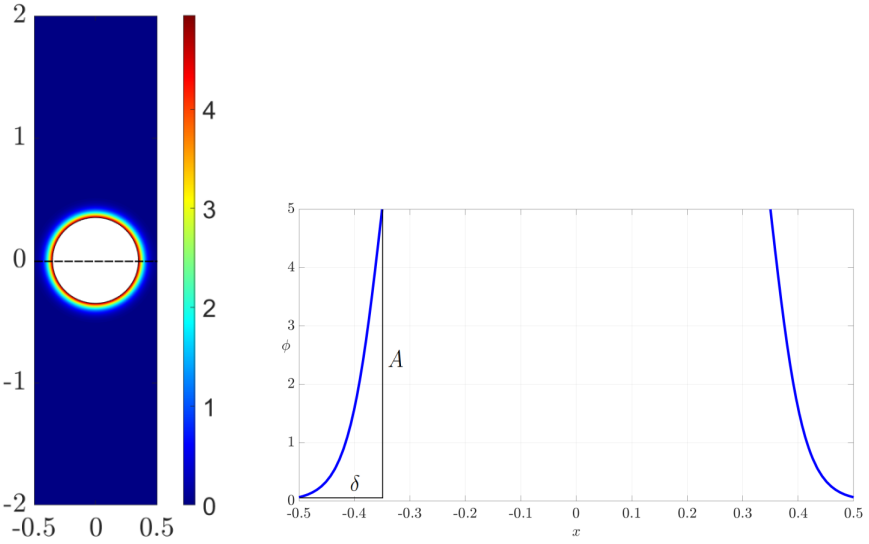

(a) Isocontour ϕ *(b) $\phi - x$*

Fig. 7.1: a) is the isocontour of the potential ϕ. b) is the behaviour of ϕ along the dashed black line in the isocontour. A, δ are the parameters in (7.1).

7.1 Microscopic configuration 1

In this case we specify the concentration flux in equation (6.1) as

$$A(x) = n_x + 5. \tag{7.2}$$

The microscopic resulting fields are shown in figure 7.2, while their averages in tables 7.1 and 7.2.

	T_n	Y_n
$\dot{-}\mathbb{U}$	2.5930×10^{-2}	-2.0151×10^{-6}
$\dot{-}\mathbb{D}$	2.0151×10^{-6}	-2.5930×10^{-2}

Tab. 7.1: Non-zero averaged components of T and Y

	γ	A_n	B_n	a_n
$\dot{-}\mathbb{U}$	5.03×10^{-2}	5.87×10^{-5}	5.87×10^{-5}	-5.22×10^{-5}
$\dot{-}\mathbb{D}$	6.97×10^{-2}	5.87×10^{-5}	5.87×10^{-5}	-5.22×10^{-5}

Tab. 7.2: Non-zero averaged components of γ, A, B and a

The problems for M and N are the same as in the short range potential limit and the solution is not presented here.

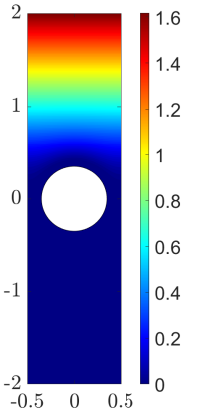

(a) T_n

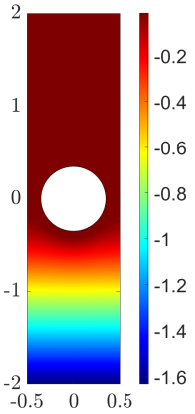

(b) Y_n

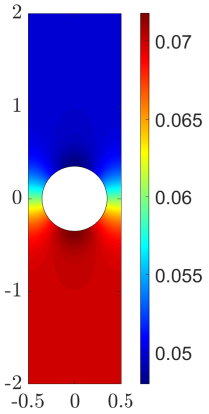

(c) γ

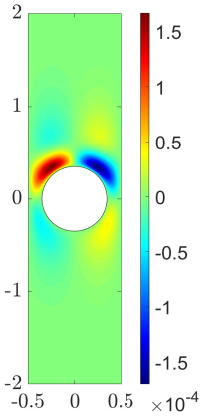

(d) A_t

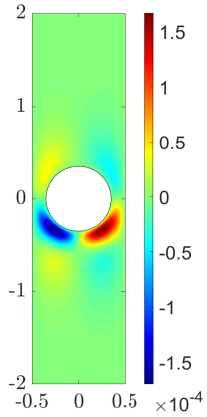

(e) B_t

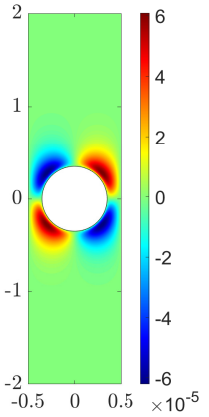

(f) a_t

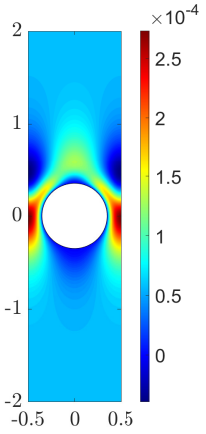

(g) A_n

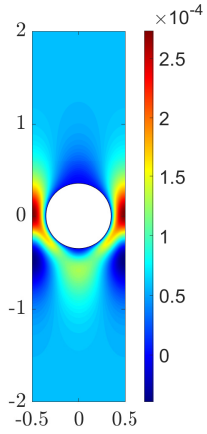

(h) B_n

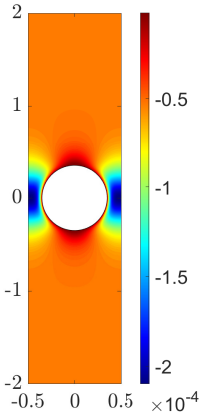

(i) a_n

Fig. 7.2: Microscopic fields for the potential defined in equation 7.1 and the concentration flux specified by 7.2.

	γ	a_t	a_n
$\dot{-}\mathbb{U}$	5.31×10^{-2}	-6.19×10^{-5}	-3.63×10^{-5}
$\dot{-}\mathbb{D}$	6.69×10^{-2}	-6.19×10^{-5}	-3.63×10^{-5}

Tab. 7.3: γ and a_i with $A(x)$ defined in equation (7.3)

7.2 Microscopic configuration 2

A second microscopic configuration is considered, with $A(x)$ such that

$$A(x) = cos(\frac{\pi}{4})n_x + sin(\frac{\pi}{4})n_y + 5. \tag{7.3}$$

The microscopic fields, solution of problems (6.9–6.13) are shown in figure 7.3, while their averages in table 7.3. The solutions of the microscopic problems not affected by changes in A are not shown.

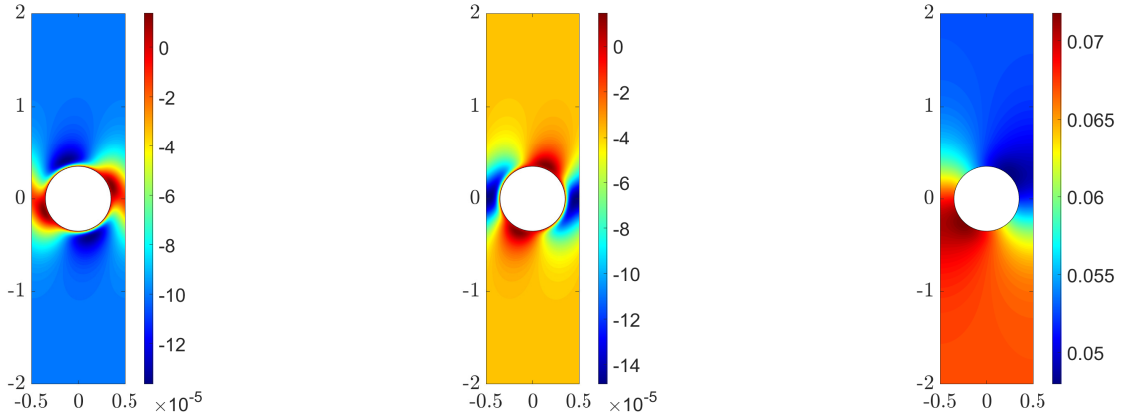

(a) a_t *(b) a_n* *(c) γ*

Fig. 7.3: Microscopic solution of problems with A defined in equation (7.3)

8 Long range potential limit: macroscopic solution and validation

Once the microscopic tensors have been obtained from problems (6.9, 6.10, 6.11, 6.12) and (6.13), the macroscopic interface condition (6.14, 6.15, 6.16) and (6.17) is used to solve for a specific flow configuration. The solution of the macroscopic model is validated by comparisons against the full-scale flow solution. A square domain of size $2L$x$2L$ as sketched in figure 8.1, is considered.

We impose a no slip condition on the boundaries of the domain except for the two upper openings denoted by Π_L and Π_R where the fluid freely flows. We impose the potential introduced in equations (7.1) on the solid walls of the full-scale membrane, and vary the concentration flux on $\partial\mathbb{M}$ according to equations (7.2) or (7.3).

In the flow configurations analysed, the DNS and the macroscopic model are in good agreement.

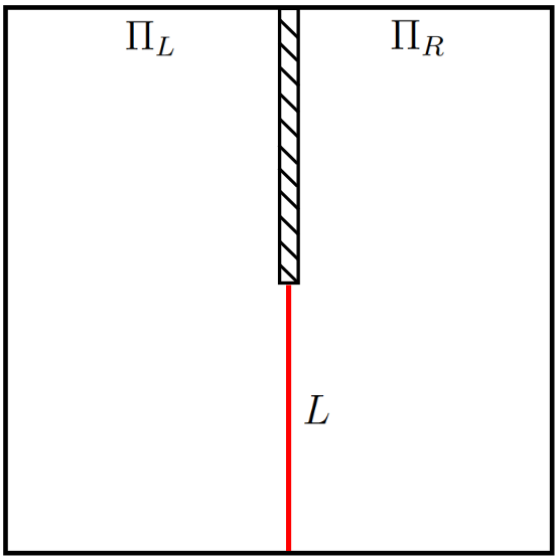

Fig. 8.1: Sketch of the macroscopic domain. The red line represents the membrane, the black lines represent the boundaries of the domain, while the dashed rectangle is a wall that split the fluid domain in two parts.

8.1 Validation Case 1

In this configuration, (7.2) is imposed on the membrane walls $\partial\mathbb{M}$. The outflow conditions $\partial_n u_i = 0$ and $\partial_n c = 0$ are imposed on Π_L and Π_R.

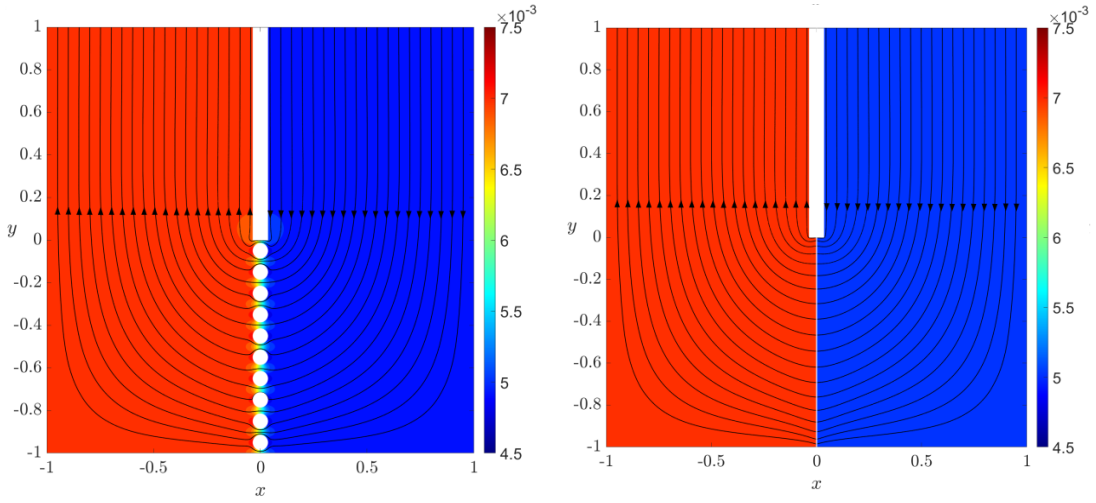

(a) DNS *(b) Macroscopic solution*

Fig. 8.2: Isocontours of concentration with the flow streamlines. Frame (a): solution of the full-scale equation (6.3). Frame (b): solution of the macroscopic model (6.14,6.15,6.16,6.17). Streamlines are in black. In frame (a) the white circles are the inclusion. In frame (b) the vertical white line represents the equivalent macroscopic membrane ($y \in [-1, 0]$).

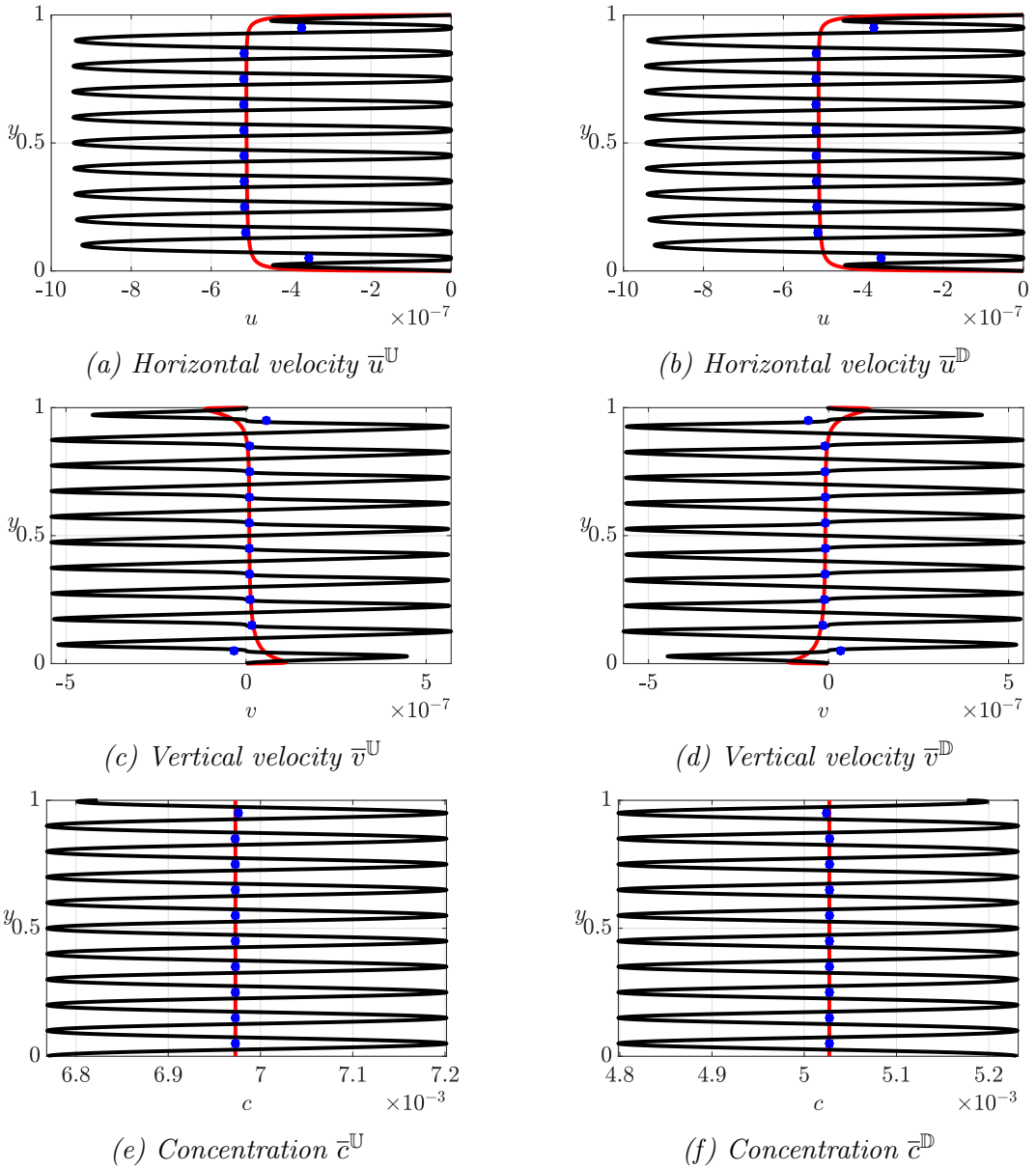

(a) Horizontal velocity $\overline{u}^{\mathbb{U}}$

(b) Horizontal velocity $\overline{u}^{\mathbb{D}}$

(c) Vertical velocity $\overline{v}^{\mathbb{U}}$

(d) Vertical velocity $\overline{v}^{\mathbb{D}}$

(e) Concentration $\overline{c}^{\mathbb{U}}$

(f) Concentration $\overline{c}^{\mathbb{D}}$

Fig. 8.3: Quantitative comparison for ε=0.05. Horizontal velocities (a,b), vertical velocities (c,d) and concentrations (e,f) evaluated along the membrane. Frames (a,c,e) refer to $\overline{\cdot}^{\mathbb{U}}$ (3.16). Frames (b,d,f) refer to the $\overline{\cdot}^{\mathbb{D}}$ (3.16). Black profiles refer to the solution of full-scale equations (6.3). The solid red lines refer to the solution of the macroscopic model (6.14–6.17). The blue points represent the average of the full-scale solution.

8.2 Validation Case 2

In this configuration equation (7.3) is imposed on the membrane walls $\partial\mathbb{M}$. A positive macroscopic vertical velocity is generated.

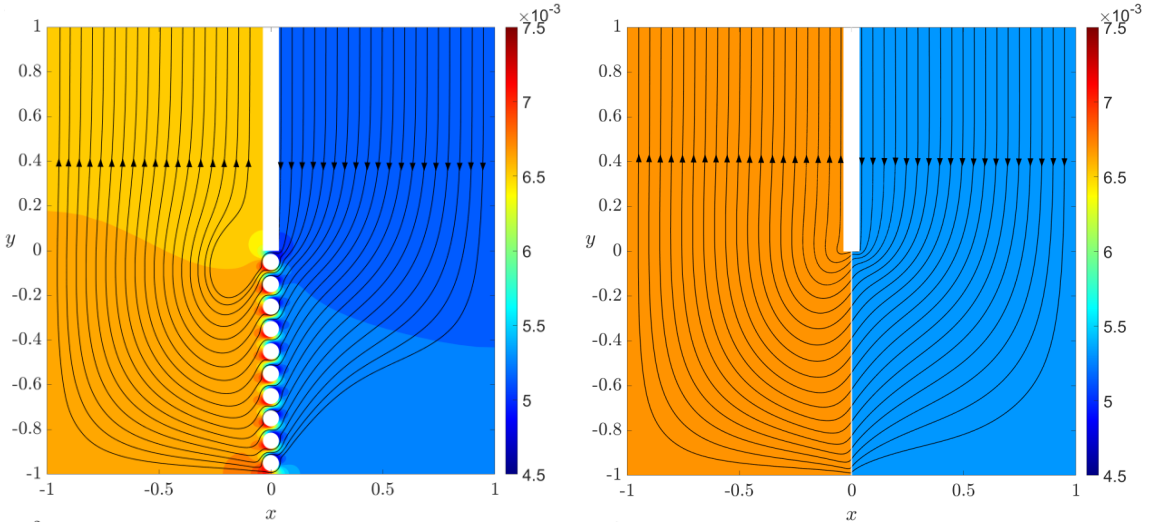

(a) DNS *(b) Macroscopic model*

Fig. 8.4: Isocontours of concentration with the flow streamlines. Frame (a): solution of the full-scale equation (6.3). Frame (b): solution of the macroscopic model (6.14,6.15,6.16,6.17). Streamlines are in black. In frame (a) the white circles are the inclusions. In frame (b) the vertical white line represents the equivalent macroscopic membrane ($y \in [-1, 0]$).

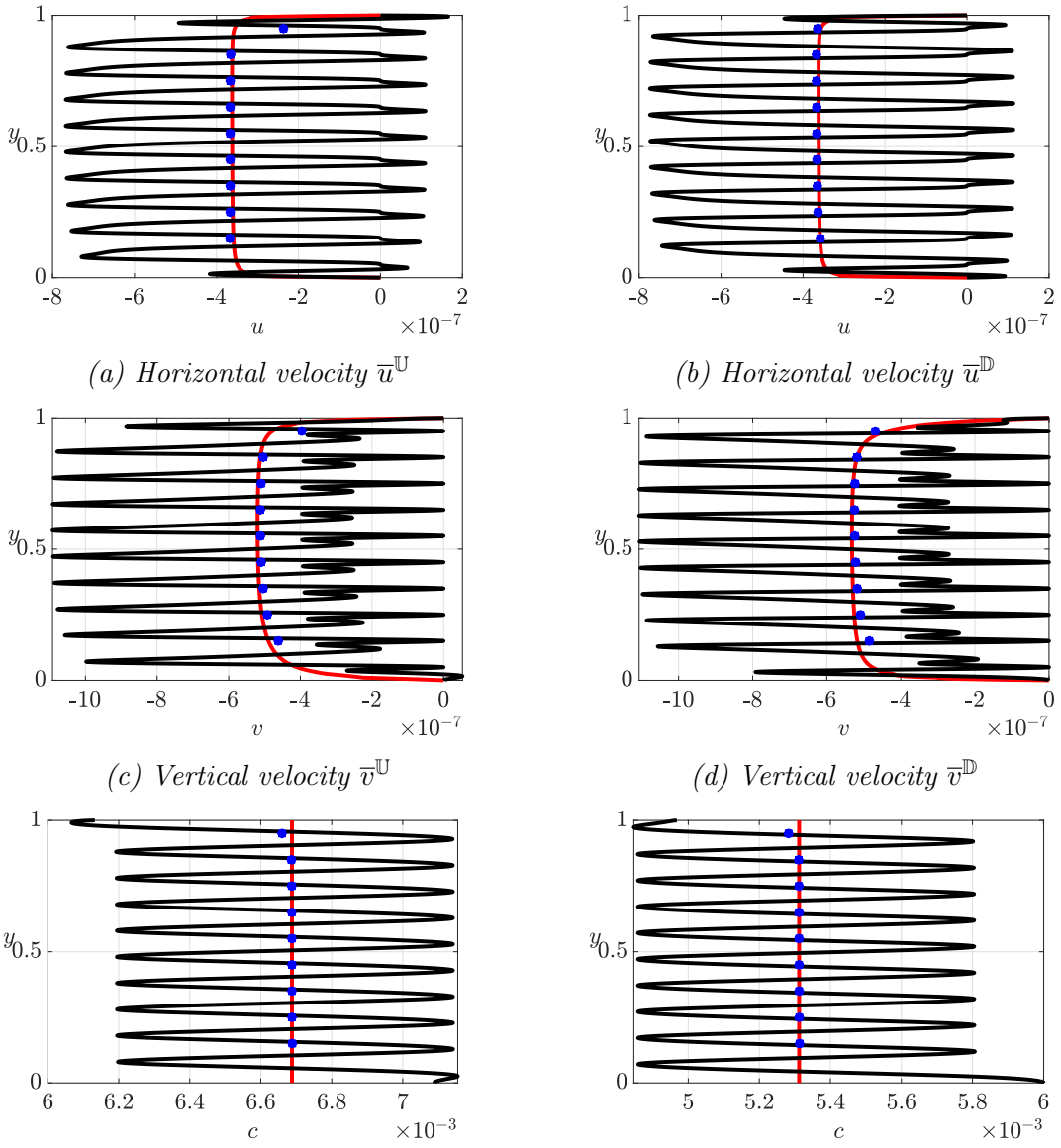

(a) Horizontal velocity $\overline{u}^{\mathbb{U}}$ *(b) Horizontal velocity $\overline{u}^{\mathbb{D}}$*

(c) Vertical velocity $\overline{v}^{\mathbb{U}}$ *(d) Vertical velocity $\overline{v}^{\mathbb{D}}$*

(e) Concentration $\overline{c}^{\mathbb{U}}$ *(f) Concentration $\overline{c}^{\mathbb{D}}$*

Fig. 8.5: Quantitative comparison for ε=0.05. Horizontal velocities (a,b), vertical velocities (c,d) and concentrations (e,f) evaluated along the membrane. Frames (a,c,e) refer to $\overline{\cdot}^{\mathbb{U}}$ (3.16). Frames (b,d,f) refer to the $\overline{\cdot}^{\mathbb{D}}$ (3.16). Black profiles refer to the solution of full-scale equations (6.3). The solid red lines refer to the solution of the macroscopic model (6.14–6.17). The blue points represent the average of the full-scale solution.

8.3 Towards the modelling of osmotic flows

In this configuration, $A(x) = 0$ on the membrane walls while a Dirichlet condition has been imposed for the concentration on Π_L (cf. figure 8.1, c=1). Imposing a null concentration flux at the membrane wall is the most common way to account for semipermeable membranes [20]. The case considered here hence represent a macroscopic calculation of an osmotic flow.

The model is able well predict the concentration and velocity along the membrane.

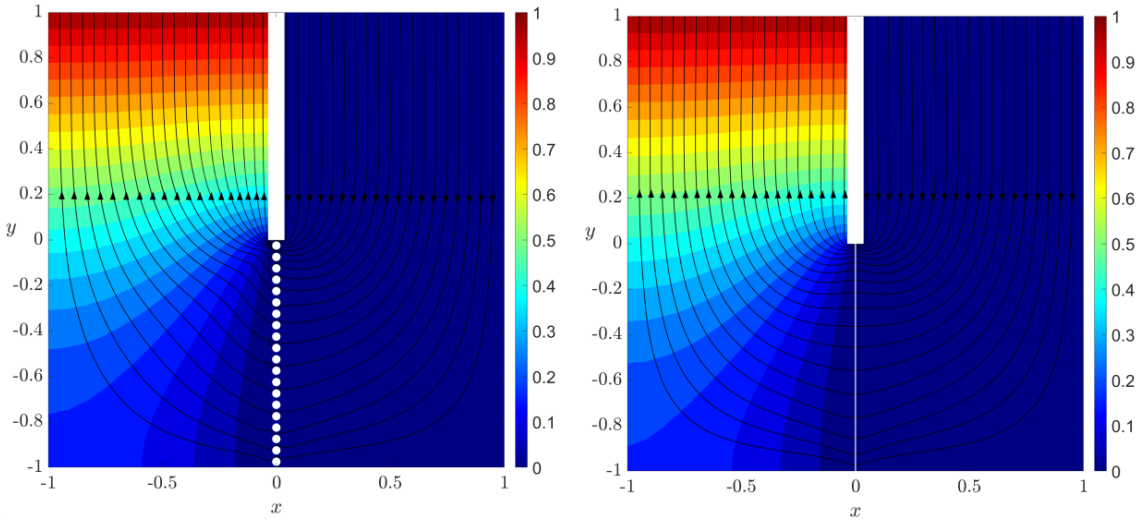

(a) DNS *(b) Macroscopic model*

Fig. 8.6: Isocontours of concentration with the flow streamlines. Frame (a): solution of the full-scale equation (6.3). Frame (b): solution of the macroscopic model (6.14,6.15,6.16,6.17). Streamlines are in black. In frame (a) the white circles are the inclusion. In frame (b) the vertical white line represents the equivalent macroscopic membrane ($y \in [-1, 0]$).

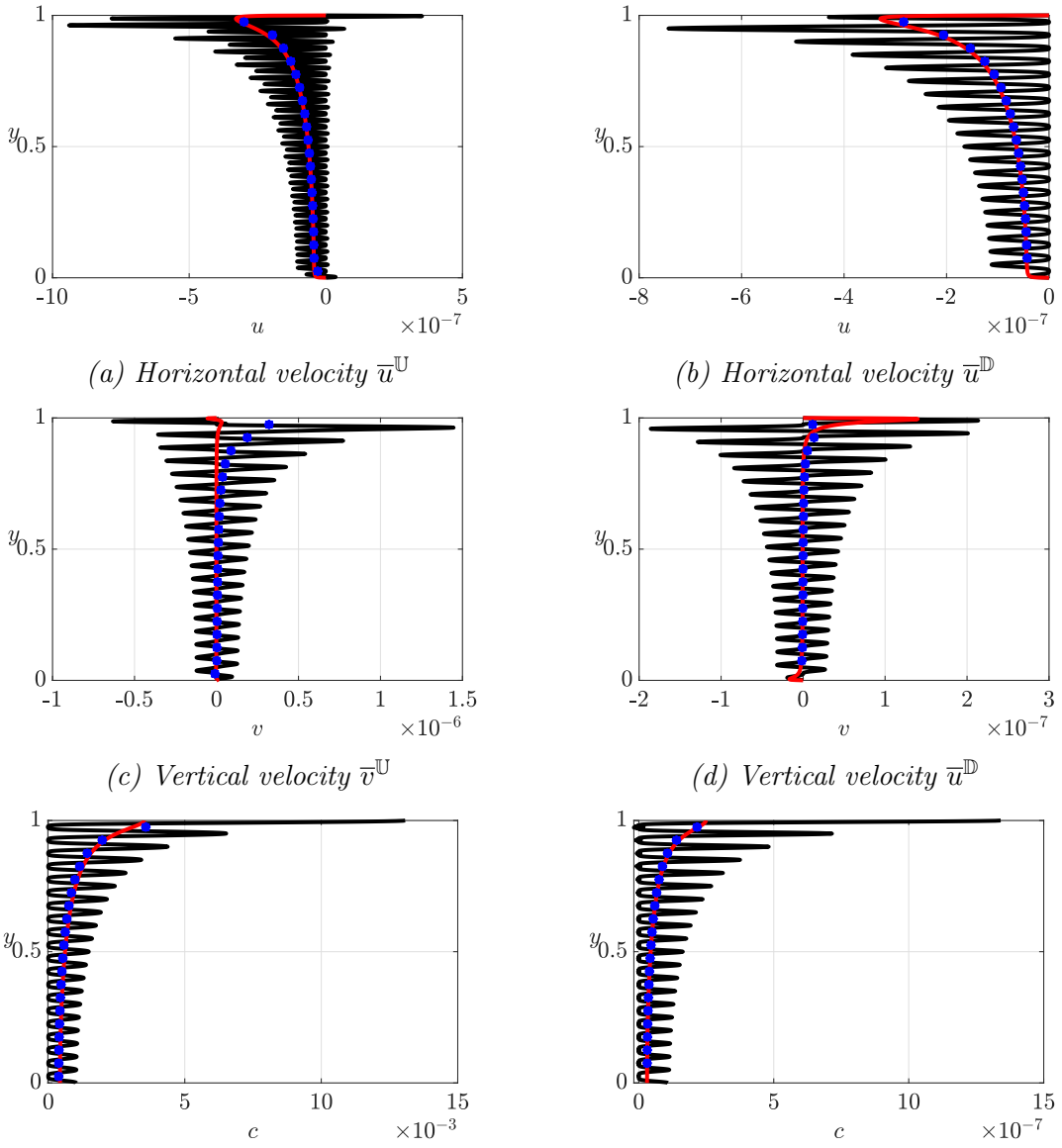

(a) Horizontal velocity $\overline{u}^{\mathbb{U}}$ *(b) Horizontal velocity $\overline{u}^{\mathbb{D}}$*

(c) Vertical velocity $\overline{v}^{\mathbb{U}}$ *(d) Vertical velocity $\overline{u}^{\mathbb{D}}$*

(e) Concentration $\overline{c}^{\mathbb{U}}$ *(f) Concentration $\overline{c}^{\mathbb{D}}$*

Fig. 8.7: Quantitative comparison for ε=0.05. Horizontal velocities (a,b), vertical velocities (c,d) and concentrations (e,f) evaluated along the membrane. Frames (a,c,e) refer to $\overline{\cdot}^{\mathbb{U}}$ (3.16). Frames (b,d,f) refer to the $\overline{\cdot}^{\mathbb{D}}$ (3.16). Black profiles refer to the solution of full-scale equations (6.3). The solid red lines refer to the solution of the macroscopic model (6.14–6.17). The blue points represent the average of the full-scale solution.

9 Conclusions

In the present work we have developed a homogeneous model to simulate the phoretic effects of micro-structured surfaces on a surrounding fluid. On the basis of the phoretic properties of the membrane, we distinguish between the short and long potential limit, and two corresponding models are found. The models are purely macroscopic, i.e. they account for the presence of the micro-structure via a flow constraint imposed on a smooth single-scale interface between two fluid regions. On the interface, the fluid-solid couple behaves as a new continuum with effective properties different from those of the initial fluid.

Within the short range potential hypothesis, we were able to represent the phoretic contribution to the flow as a slip velocity on the solid walls of the membrane. The slip velocity depends on the concentration gradient on $\partial\mathbb{M}$. Macroscopically, the velocity and the concentration are described by a linear combination of the upward and downward stress tensors and solute fluxes, plus some coefficients which represent the upscaled phoretic contribution to the flow. The coefficients present in the macroscopic condition are the averaged entries of tensors retrieved by the solution of Stokes and Laplace problems within a microscopic domain.

The model, which allows us to evaluate the effects of the microstructured surface on the macroscopic flow, shows a high degree of generality regarding (i) the microscopic topology of the membrane (only periodicity along the tangential to the surface direction is assumed) and (ii) the macroscopic shape of the membrane (whose only constraint is $l/L{=}\varepsilon$). A third important aspect relates to the fact that the condition is applicable to generic flow configurations.

In the case of long range potential, a volumetric term in the Navier-Stokes equations is added. The macroscopic model exhibits a structure similar to the short range potential limit, while the microscopic coefficients solve modified microscopic problems.

After a validation of the model against fully-resolved simulations, we have shown that the desired flow pattern may arise from the interplay between the macroscopic membrane geometry and the microscopic phoretic properties of the inclusions.

In the last chapter of the thesis, the macroscopic model has been applied to analyze osmotic flows, showing a good agreement with the full-scale solution.

In the present work we considered neutral solutions, the application of the same procedure to electrolytes, will lead to the macroscopic description of electrophoresis and electrosmosis.

The model developed applies to those situations where the pore size is such that continuum Stokes and advection diffusion equations are valid, (cf., for instance, the flow of aqueous solutions through sieve tubes [21, 22]). Important biological processes happen at smaller scales, across subnanometric pores (cf., for instance, [23]) and the initial equations of the homogenization procedure should be modified to account for confinement effects [24].

References

[1] G. M. Whitesides. The origins and the future of microfluidics. *Nature*, 442(7101):368–373, 2006.

[2] S. K. Sia and G. M. Whitesides. Microfluidic devices fabricated in poly (dimethylsiloxane) for biological studies. *Electrophoresis*, 24(21):3563–3576, 2003.

[3] M. A. Chilvers and C. O'callaghan. Local mucociliary defence mechanisms. *Paediatric respiratory reviews*, 1(1):27–34, 2000.

[4] J. den Toonder, F. Bos, D. Broer, L. Filippini, M. Gillies, J. de Goede, T. Mol, M. Reijme, W. Talen, H. Wilderbeek, et al. Artificial cilia for active microfluidic mixing. *Lab on a Chip*, 8(4):533–541, 2008.

[5] A. Babataheri, M. Roper, M. Fermigier, and O. Du Roure. Tethered fleximags as artificial cilia. *Journal of Fluid Mechanics*, 678:5–13, 2011.

[6] E. Lauga and T. R. Powers. The hydrodynamics of swimming microorganisms. *Reports on progress in physics*, 72(9):096601, 2009.

[7] S. N. Khaderi, J. M. J. Den Toonder, and P. R. Onck. Microfluidic propulsion by the metachronal beating of magnetic artificial cilia: a numerical analysis. *Journal of fluid mechanics*, 688:44–65, 2011.

[8] S. N. Khaderi, J. M. J. Den Toonder, and P. R. Onck. Fluid flow due to collective non-reciprocal motion of symmetrically-beating artificial cilia. *Biomicrofluidics*, 6(1):014106, 2012.

[9] S. Michelin, T. D. Montenegro-Johnson, G. De Canio, N. Lobato-Dauzier, and E. Lauga. Geometric pumping in autophoretic channels. *Soft matter*, 11(29):5804–5811, 2015.

[10] J. L. Anderson. Colloid transport by interfacial forces. *Annual review of fluid mechanics*, 21(1):61–99, 1989.

[11] W. F. Paxton, K. C. Kistler, C. C. Olmeda, A. Sen, S. K. St. Angelo, Y. Cao, T. E. Mallouk, P. E. Lammert, and V. H. Crespi. Catalytic nanomotors: autonomous movement of striped nanorods. *Journal of the American Chemical Society*, 126(41):13424–13431, 2004.

[12] J. R. Howse, R. A. Jones, A. J. Ryan, T. Gough, R. Vafabakhsh, and R. Golestanian. Self-motile colloidal particles: from directed propulsion to random walk. *Physical review letters*, 99(4):048102, 2007.

[13] J. Palacci, S. Sacanna, A. P. Steinberg, D. J. Pine, and P. M. Chaikin. Living crystals of light-activated colloidal surfers. *Science*, 339(6122):936–940, 2013.

[14] S. Michelin and E. Lauga. Universal optimal geometry of minimal phoretic pumps. *Scientific reports*, 9(1):1–7, 2019.

[15] T. Yu, A. G. Athanassiadis, M. N. Popescu, V. Chikkadi, A. Gäth, D. P. Singh, T. Qiu, and P. Fischer. Microchannels with self-pumping walls. *ACS nano*, 14(10):13673–13680, 2020.

[16] G. A. Zampogna, P. G. Ledda, and F. Gallaire. Transport across thin membranes: Effective solute flux jump. *Physics of Fluids*, 34(8):083113, 2022.

[17] C. C. Mei and B. Vernescu. *Homogenization methods for multiscale mechanics*. World scientific, 2010.

[18] B. J. Kirby. *Micro-and nanoscale fluid mechanics: transport in microfluidic devices*. Cambridge university press, 2010.

[19] S. Michelin and E. Lauga. Phoretic self-propulsion at finite péclet numbers. *Journal of fluid mechanics*, 747:572–604, 2014.

[20] T. Gebäck and A. Heintz. A pore scale model for osmotic flow: homogenization and lattice boltzmann simulations. *Transport in Porous Media*, 126:161–176, 2019.

[21] Y. Liu, H. Xu, W. Dai, H. Li, and W. Wang. 2.5-dimensional parylene c micropore array with a large area and a high porosity for high-throughput particle and cell separation. *Microsystems & Nanoengineering*, 4(1):13, 2018.

[22] K. H. Jensen, K. Berg-Sørensen, H. Bruus, N. M. Holbrook, J. Liesche, A. Schulz, M. A. Zwieniecki, and T. Bohr. Sap flow and sugar transport in plants. *Reviews of modern physics*, 88(3):035007, 2016.

[23] A. S. Verkman. Aquaporins in clinical medicine. *Annual review of medicine*, 63:303–316, 2012.

[24] S. Gravelle, L. Joly, F. Detcheverry, C. Ybert, C. Cottin-Bizonne, and L. Bocquet. Optimizing water permeability through the hourglass shape of aquaporins. *Proceedings of the National Academy of Sciences*, 110(41):16367–16372, 2013.

[25] P. R. Amestoy, I. S. Duff, J. L'Excellent, and J. Koster. Mumps: a general purpose distributed memory sparse solver. In *Applied Parallel Computing. New Paradigms for HPC in Industry and Academia: 5th International Workshop, PARA 2000 Bergen, Norway, June 18–20, 2000 Proceedings 5*, pages 121–130. Springer, 2001.

[26] A. Quarteroni and A. Valli. *Domain Decomposition Methods for Partial Differential Equations*. Oxford University Press, Oxford, UK, 1999.

A Appendix

A.1 COMSOL Multiphysics

COMSOL Multiphysics is a numerical simulation software based on the finite element method. This software has been designed to simulate many physics and engineering applications, and in particular coupled phenomena or multiphysics simulations.
All the microscopic and macroscopic problems are implemented using the weak form PDE tool. To obtain the weak form, the PDEs are integrated in the domain they belong to, multiplied by a test function and then integrated by parts.

P2-P1 Taylor-Hood elements have been employed for the discretization of the hydrodynamic micro and macroscopic equations. Quadratic elements have been used for the solution of Laplace and advection diffusion problems. The MUMPS solver [25] to carry out the solution of the linear systems deriving from the spatial discretization has been employed.

Regarding the implementation of the macroscopic solutions, we use the domain decomposition method [26]. The problem is decoupled between the upward $\mathbb{U}$ and downward $\mathbb{D}$ regions (cf. sketch A.1) where Stokes (2.1) and advection-diffusion (2.2) equations are solved. The two sets of equations are then coupled via the interface conditions (3.8) on the macroscopic membrane $\mathbb{C}$.

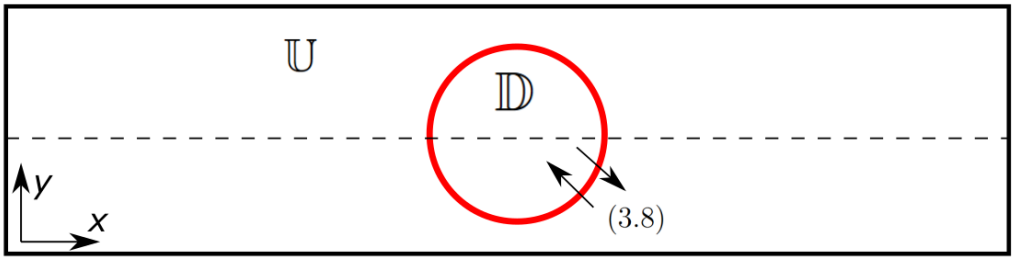

Fig. A.1: Sketch of the domain decomposition method for the configuration 2 in chapter 5.

A.2 Domain and mesh size invariance

To obtain numerically consistent results, the invariance of the microscopic and macroscopic solutions with respect to the size of the cells forming the mesh has been tested. The variation of the averages of the microscopic tensors with the cells size are shown in figure A.2.

From a theoretical point of view, the normal to the membrane size of the microscopic elementary cell tends to infinity (cf. figure A.3). The invariace of the microscopic results with respect to the cell size has been verified (cf. figure A.4).

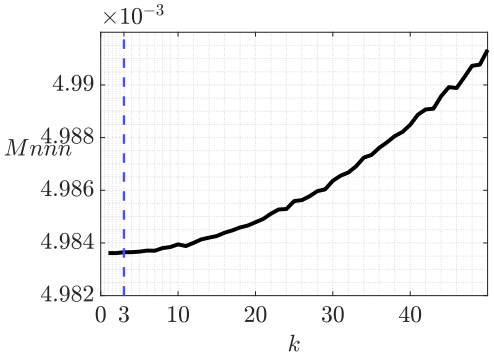

Fig. A.2: $\overline{M}^{\mathbb{U}}_{nnn}$ is plotted by varying the value of the coefficient k. k is associeted with the cell size. For k smaller than 3, which corresponds to a cell size equal to $0.05l$, $\overline{M}^{\mathbb{U}}_{nnn}$ reaches an asymptotic value.

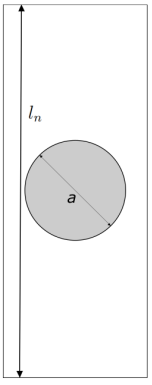

Fig. A.3: Sketch of the microscopic domain with the definition of the parameter l_n.

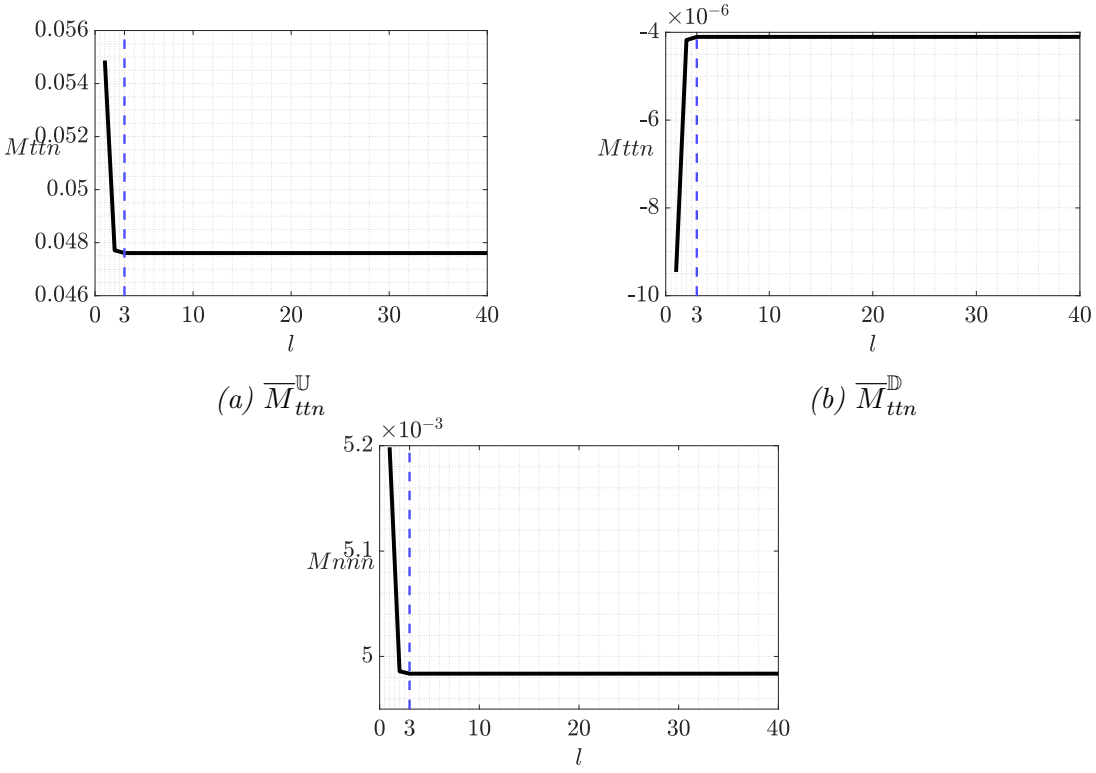

(a) $\overline{M}^{\mathbb{U}}_{ttn}$ *(b)* $\overline{M}^{\mathbb{D}}_{ttn}$

(c) $\overline{M}^{\mathbb{U}}_{nnn}$

Fig. A.4: Effective coefficients $\overline{M}^{\mathbb{U}}_{ttn}$, $\overline{M}^{\mathbb{D}}_{ttn}$ *for variations of* l_n. *After* $l - n = 3$ *(dashed blue lines) the effective coefficients reach an asymptotic value. The results presented in the thesis have been carried out using* $l_n = 4$.